GEORG-AUGUST-UNIVERSITÄT
GÖTTINGEN

Fakultät für
Physik

Bachelor's Thesis

Implementierung eines Algorithmus zur Feineinstellung der Diskriminatorschwelle für Silizium- und Diamant-Pixeldetektoren

Implementation of a Threshold Tuning Algorithm for Silicon and Diamond Pixel Detectors

prepared by

Maria Mironova

from Göttingen

at the II. Physikalischen Institut

Thesis number:	II.Physik-UniGö-BSc-2017/02
Thesis period:	27th March 2017 until 3rd July 2017
First referee:	Prof. Dr. Arnulf Quadt
Second referee:	Priv.Doz. Dr. Jörn Große-Knetter

Contents

1 Introduction

The Large Hadron Collider (LHC) at CERN is currently the main instrument in high energy physics for investigating the fundamental properties of matter. In 2012, the two LHC experiments ATLAS and CMS provided evidence for the final missing particle in the Standard Model (SM), the Higgs boson [1] [2]. Nevertheless, the SM is far from a complete understanding of particle physics. Different experimental observations, in particular in cosmology, suggest that the SM is not a complete description of matter, making the search for beyond Standard Model (BSM) particles one of the main objectives of the LHC and its detectors.

Current theories predict that these BSM particles possess much higher masses than the known particles in the SM. As a consequence, colliders have to provide very high energies to produce such particles. At a fixed center of mass energy, processes become less likely if they require high energies. As a consequence, a large number of collisions, a quantity related to a high luminosity, is needed. For the study of the physics behind the processes that occur in the LHC, detectors are needed, to identify particles and reconstruct particle tracks, for example multi-purpose detectors such as ATLAS and CMS. An integral part of the detectors is the tracking detector, that measures the track of a particle in a magnetic field, providing information about its momentum. This detector is located very close to the collision point and therefore has to fulfill special requirements. A large number of particles traverse the detector every second and it is important that the detector can quickly identify hits and transmit a signal without missing information. The detector has to provide good information over the course of the lifetime of the LHC. This means that the detector components have to be very resistant to radiation damage.

The most commonly used sensor material in tracking detectors is silicon, but in the light of the upgrade to higher luminosities at the LHC other options are considered. One possibility is the use of diamond pixel detectors, that are very radiation tolerant, but the use of diamond leads to a smaller signal, which poses a new challenge to the readout of the sensor. In this project a new threshold tuning algorithm was implemented into the readout

software of pixel detectors, to allow setting a much lower threshold. In comparison to the previous tuning mechanism, which used charge injection, the new algorithm measures the noise in the sensor and then sets the threshold to be slightly above the noise floor. The algorithm was tested for silicon pixel sensors and can later be applied to diamond sensors.

2 Theoretical Background

2.1 The Standard Model

The Standard Model of Particle Physics describes the current knowledge of elementary particles and their interactions. It contains 17 particles, that may be divided into fermions and bosons, as shown in Fig. 2.1.

The fermions are spin-1/2 particles and may be understood as the constituents of matter, whilst the spin-1 bosons are the mediators of the fundamental forces. In the SM these are the electromagnetic, strong and weak interactions. The strong and electromagnetic interactions are mediated by massless particles, the photon (γ) and the gluon (g), respectively. In contrast, the force carriers of the weak interaction are the heavy W^+, W^- and Z bosons.

In general, the SM consists of three generations of particles; with increasing generation the particles become heavier but share all of the other properties of their respective first generation particle, such as spin and charge. Due to their larger masses, the heavy particles are unstable and decay into their first generation equivalents, meaning that all stable matter consists only of particles from the first generation.

The fermionic part of the SM may be divided into quarks, charged and neutral leptons (neutrinos). Neutrinos are neutral particles with small rest masses, $m_\nu < 2$ eV [3]. They may only interact via the weak interaction and are thus hard to observe experimentally. The charged leptons are the electron, muon and tau, each with a charge of -1 e, with e representing the unit charge of $1.602 \cdot 10^{-19}$ C, allowing them to interact via the electromagnetic force. The remaining six elementary particles are the quarks, with the up-type quarks having charges of $+\frac{2}{3}$ e and the down-type quarks having charges of $-\frac{1}{3}$ e. In addition to the weak and electromagnetic forces, the quarks have a colour charge, which allows them to interact using the strong force. Due to the nature of the strong force, quarks can only be found in colour neutral combinations, either in baryons (three-quark-particles) or mesons (quark-antiquark-particles).

The most recent discovery in the SM is the Higgs boson [1][2]. The Higgs is a spin 0 boson and represents an excitation of the Higgs field. The interaction with this field is

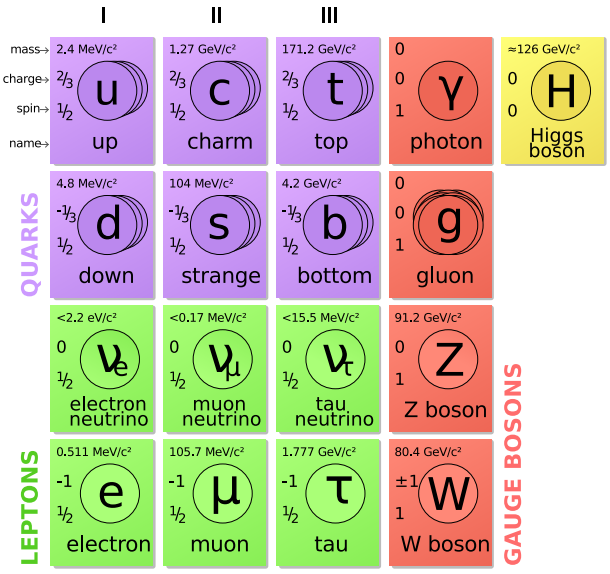

Figure 2.1: The Standard Model of Particle Physics.

what gives mass to particles. The Higgs mechanism was proposed in the 1960s and the Higgs boson was discovered by the ATLAS and CMS experiments in 2012.

The SM combines all current knowledge of the fundamental particles. Nevertheless, there are multiple phenomena which cannot be explained by the SM. As a consequence, there are several Beyond Standard Model (BSM) theories that require further investigation with high energy experiments. Current issues with the SM include:

Gravity

Gravity is currently not included in the SM. For particles it is a reasonable approximation to neglect gravity, since it is 41 orders of magnitude weaker than the electromagnetic interaction on the scale of quarks. Apart from the desire to form a model that also includes gravity, general relativity and quantum mechanics are not compatible on the Planck scale, where both become relevant.

Dark Matter and Dark Energy

Observations of galaxy rotation curves show a distribution of radial velocities that cannot be explained using current models. This is one of the indications that there must be heavy, weakly interacting matter that cannot be observed with our current methods. One possible explanation is supersymmetry (SUSY), a theory that predicts the existence of such heavy particles. Currently, the search for BSM particles is one of the main objectives of high energy physics.

Aesthetic Issues of the SM

Aside from observations that point towards physics beyond the Standard Model, there are some issues which are not critical but where a solution would be desirable from a theoretical viewpoint, for example the Hierarchy Problem. When considering the Higgs boson mass, quantum loop corrections have to be made. For high energies these corrections can become very large and as a consequence, one would expect a Higgs mass on the Planck scale. The explanation for a much lower observed Higgs mass requires a lot of fine tuning. A much easier solution can, for example, be provided by SUSY.

2.2 Experimental Particle Physics

2.2.1 The LHC

The Large Hadron Collider (LHC) [4] is a proton-proton collider at CERN with a circumference of 26.7 km, making it the worlds largest accelerator, and hence the currently most important instrument for particle physics research. The LHC can run at much higher beam energies than previous hadron colliders. During its first run, the beam energy reached 3.5 TeV, giving a center of mass energy of $\sqrt{s} = 7$ TeV. For the current second run the beam energy is even higher with 6.5 TeV, so $\sqrt{s} = 13$ TeV. When considering a collider, another important property is the luminosity that describes the number of particle collisions per time and area. For the first run of the LHC the luminosity was $\mathcal{L} = 10^{34}$ cm^{-2}s^{-1} [4]. For the second run of the LHC, the luminosity will be even higher with $5 \cdot 10^{34}$ cm^{-2}s^{-1} [5].

In the accelerator, the two opposing proton beams cross at four interaction points, at which the four main experiments are placed: ATLAS, CMS, ALICE and LHCb. ATLAS and CMS are general purpose detectors, looking for a broad range of physical phenomena. ALICE is a detector designed to study the physics of heavy ion collisions, which are also possible in the LHC, and LHCb is a detector designed for b-physics and research on matter-antimatter-balance.

2.2.2 The ATLAS Detector

The ATLAS detector [6] consists of cylindrical detector layers as shown in Fig. 2.2. This cylindrical layout is due to the general purpose philosophy of the detector. ATLAS was designed to observe a broad range of physical phenomena, hence the detector has to cover almost the full solid angle. Due to the large number of collisions happening in the

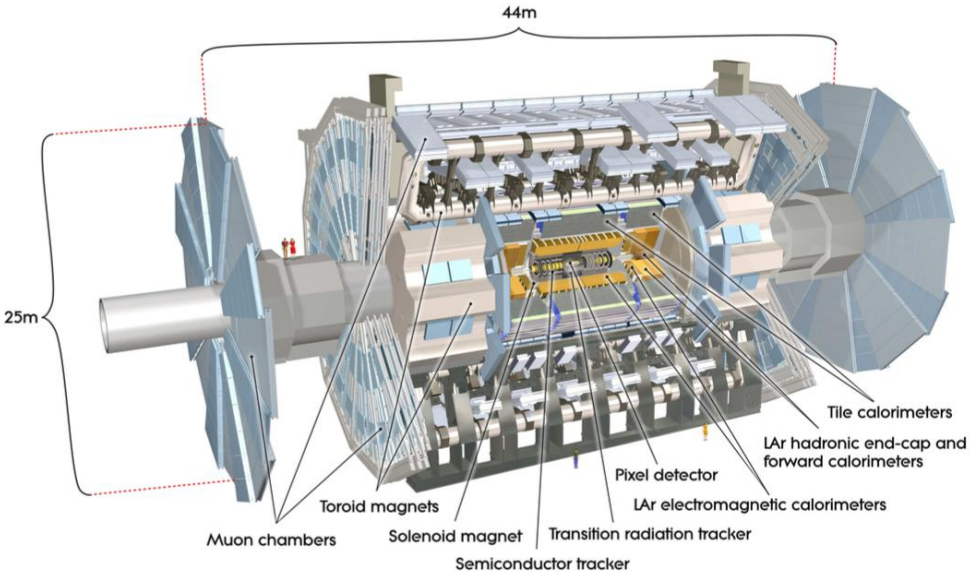

Figure 2.2: Cut-away view of the ATLAS detector [6].

LHC every second, the different detector components require fast, radiation-hard sensors and readout electronics. In addition, a good spatial resolution is required to distinguish multiple events occurring at the same time. ATLAS has a total length of 44 m, a height of 25 m and a weight of 7000 t [6]. For the coordinate system used for the ATLAS detector, the z-axis is defined to be the direction of the beam. The x-axis points towards the centre of the LHC ring and the y-axis points upwards from the interaction point. Using polar coordinates, the azimuthal angle ϕ is defined in the xy-plane and the angle θ is measured upwards from the beam axis. One important quantity in particle physics is the rapidity y, which is a measure of the direction of a particle and is defined as:

$$y = \frac{1}{2} \ln \left(\frac{E + p_L}{E - p_L} \right)$$

where E is the energy and p_L is longitudinal momentum. For ultra-relativistic particles with $p >> m$ the approximation of pseudo-rapidity $\eta = -\ln\left(\tan\left(\frac{\theta}{2}\right)\right)$ can be used. The pseudo-rapidity only depends on the polar angle θ and is useful as the intervals of pseudo-rapidity, $\Delta\eta$, are Lorentz invariant under boosts along the longitudinal axis, making it easier to compare different colliders.

Magnetic Fields

One of the methods of distinguishing particles in the ATLAS detectors is their curvature in a magnetic field, as this gives insight into the transverse momentum of a particle. The

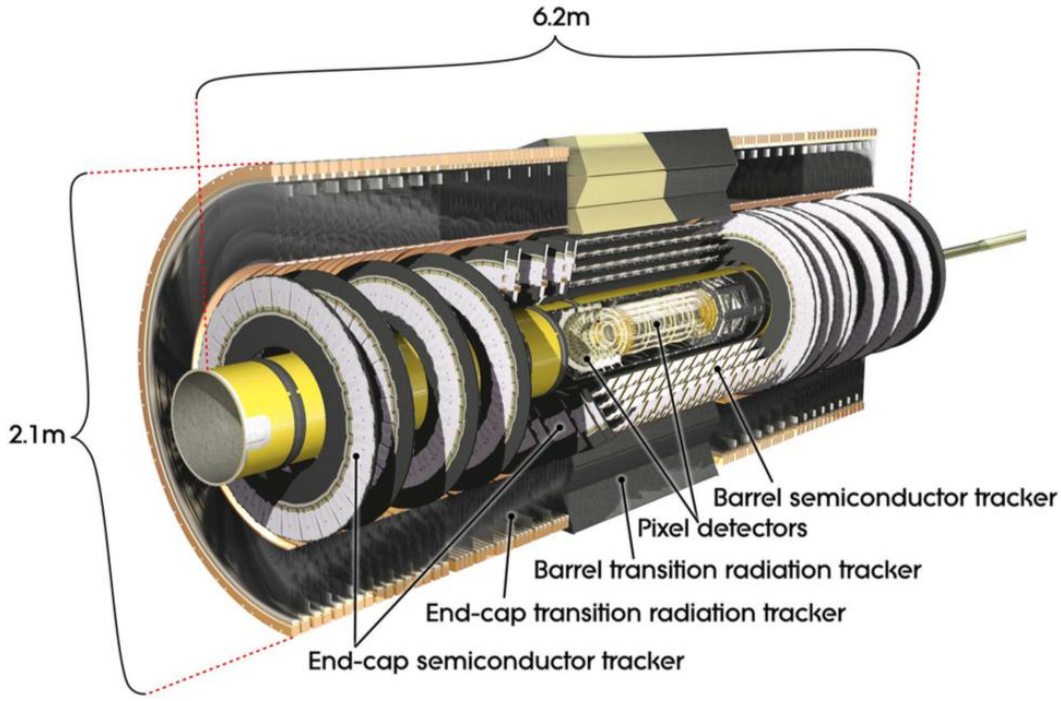

Figure 2.3: Cut-away view of the ATLAS inner detector [6].

magnet system in the ATLAS detector consists of a 2 T thin superconducting solenoid around the inner detector and three large superconducting toroids, one situated at the barrel and two at the end caps with between 0.5 and 1 T [6]. This leads to an azimuthal symmetry of the magnetic field.

Inner Detector

The Inner Detector measures the tracks of particles, allowing for the measurement of the momentum of charged particles. It consists of the Silicon Pixel Detector, the Silicon Microstrip Detector and the Transition Radiation Trackers. The Pixel Detector consists of three cylinders and three disks at the sides of the barrel, each made up of semiconducting detectors of approximately 50 μm $\times$ 400 μm [7]. The pixels provide precise spatial information about where the particle traverses the detector. The exact mechanism will be described in section 2.3.1.

The next layer of the inner detector consists of the Silicon Strip Detector. Each module of this detector consists of two layers of p-in-n microstrip sensors, the second layer of which is rotated by 40 mrad to provide a two-dimensional spatial resolution.

As shown in Fig. 2.3, the Transition Radiation Tracker (TRT) is the outer layer of the inner detector. It consists of straw-tubes in a passive material, filled with a Xenon-based

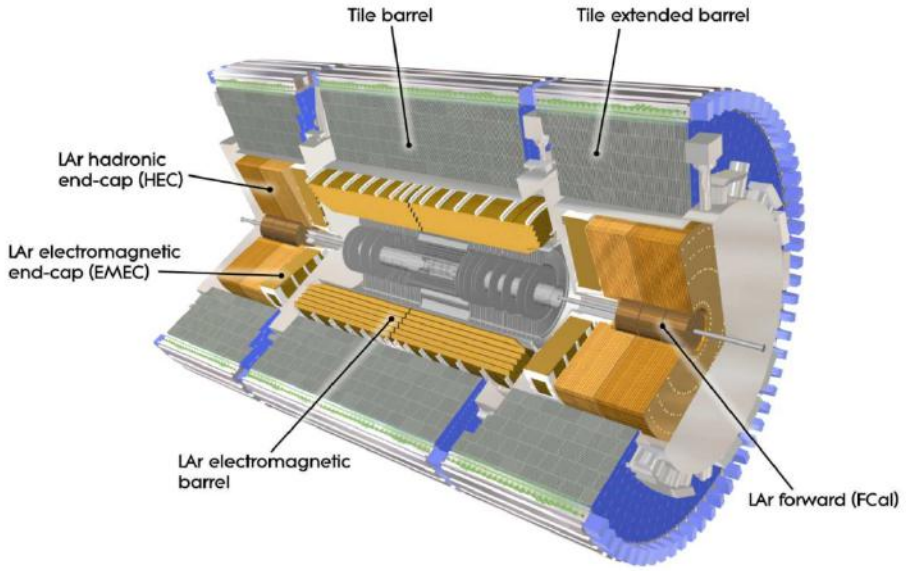

Figure 2.4: Cut-away view of the ATLAS calorimeter [6].

mixture. The tubes provide a spatial resolution of approximately 130 μm in the $r - \phi$ plane [6]. The TRT is used to identify electrons by their transition radiation. If a high-energy particle transitions from one medium into another, it emits radiation due to the change of its electric field. For particles with $\gamma > 1000$ this radiation is usually in the X-ray regime and can be detected when it is absorbed in the drift tube. The only particles with high enough γ in the LHC are the electrons, meaning they can be identified by the TRT.

Calorimeters

Following the inner detector, the next layer of ATLAS are the calorimeters. The calorimeters provide information about the energy carried by a particle. To achieve this, the particles have to be stopped completely. The first part of the calorimeters is the electromagnetic calorimeter, which can measure the energy of electrons and photons via electromagnetic showers. The next layer is the hadronic calorimeter, which is larger than the electromagnetic calorimeter, due to the larger interaction length of hadrons.

In ATLAS so-called sampling calorimeters are used, which consist of multiple layers of passive material to stop particles and active material to receive the signal. The electromagnetic calorimeters consist of layers of liquid argon as the active material and lead or steel as the passive material. The hadronic calorimeter uses steel as an absorber in the barrel region and plastic scintillators as the active material. At the end-caps (see Fig. 2.4), liquid argon is the active material and copper is the passive material. The for-

ward calorimeter (FCal) close to the beampipe has an electromagnetic part, using copper as an absorber, and a hadronic part, using tungsten as an absorber. Both parts use liquid Argon as the active material [6].

Muon Detector

The only particles that are not stopped by the calorimeter are muons and neutrinos. Neutrinos only interact weakly with matter, making them impossible to detect in ATLAS. Instead, they are reconstructed as missing transverse momentum. Muons, on the other hand, interact with matter and can be detected in the outermost part of ATLAS, specifically built to detect muons. It consists of Monitored Drift Tubes, Resistive Plate Chambers, Thin Gap Chambers and Cathode Strip Chambers. Additionally, the muon detector is placed in a toroidal magnetic field, making it possible to measure the muon momentum and reconstruct a muon track.

2.3 Pixel Sensors

2.3.1 Silicon Pixel Detectors

Interaction of Particles with Matter

To detect particles it is necessary for them to interact with matter. For semiconducting detectors, charged particles interact with the electrons of atoms through the Coulomb interaction, ionising the atoms. In this process, electrons are moved into the conduction band, leaving holes in the valence band. The average energy loss per unit distance of particles due to ionisation can be described by the Bethe-Bloch formula:

$$-\frac{1}{\rho}\left\langle\frac{dE}{dx}\right\rangle = 2\pi N_A r_e^2 m_e c^2 \frac{Z}{A}\frac{z^2}{\beta^2}\left\{\ln\left(\frac{2m_e c^2\beta^2\gamma^2 W_{max}}{I^2}\right) - 2\beta^2 - \delta - 2\frac{C}{Z}\right\} \tag{2.1}$$

where N_A is Avogadro's constant, r_e is the classical electron radius, m_e the mass of the electron, Z the atomic number of the absorbing material, A the atomic mass number, z is the charge of the incoming particle in units of e, I the mean excitation potential, W_{max} the maximum energy transfer in a single collision, C the shell correction, δ the density correction and ρ is the density of the material. The Bethe-Bloch curve has a minimum at $\beta\gamma = 3.5$, that describes the so-called minimum ionising particles (MIP). In this case,

the formula for the stopping power can be approximated to

$$-\frac{1}{\rho}\left\langle\frac{dE}{dx}\right\rangle = 1.5\ \frac{\text{MeV cm}^2}{\text{g}}. \tag{2.2}$$

This approximation is sensible for hadrons and muons in the LHC. For electrons, $\beta\gamma$ is much larger and so different processes dominate, especially Bremsstrahlung, the process in which an electron radiates a photon in the field of a nucleus.

For photons, the interactions are different as they do not carry a charge. Instead, they can interact with matter by being absorbed completely according to the photo effect. They can also be scattered by the Compton effect or be transformed into electron-positron-pairs in the field of the nucleus. The intensity of a beam decreases exponentially as it passes through a medium:

$$I(x) = I_0 e^{-\mu x} \tag{2.3}$$

where x is the distance travelled, I_0 is the initial intensity and μ is the material-specific and energy-dependent mass attenuation coefficient.

Semiconductors and pn-Transitions

In the energy-band model there are both valence and conduction bands in a material. The valence electrons are bound to the atoms whereas electrons in the conduction band are able to move freely across the material. Materials can be characterised by the energy gap between the valence band and the conduction band. For a conductor the valence and conduction band overlap, explaining the good conductivity. For insulators the valence and conduction bands are separated by a large energy gap of more than 3 eV. For a semiconductor the energy gap is usually less than 3 eV, meaning atoms can be easily ionised, leading to new additional charge carriers in the material, which can move freely. For a semiconductor the amount of signal charge carriers produced by a MIP is Q with:

$$Q = \frac{\left\langle\frac{dE}{dx}\right\rangle \rho d}{I_0} \tag{2.4}$$

where I_0 is the energy required to lift an electron into the conduction band and create an electron-hole-pair, d is the thickness of the detector and ρ is the density of the material.

For silicon, $I_0 = 3.63$ eV and $\rho = 2.329\ \text{cm}^{-3}\text{g}$, which leads to $Q = 24000e$ for $d = 250\ \mu$m [8]. This is much less than for the charge carriers which are created by thermal excitation.

However, the silicon can be doped to enhance its semiconducting properties. Doping

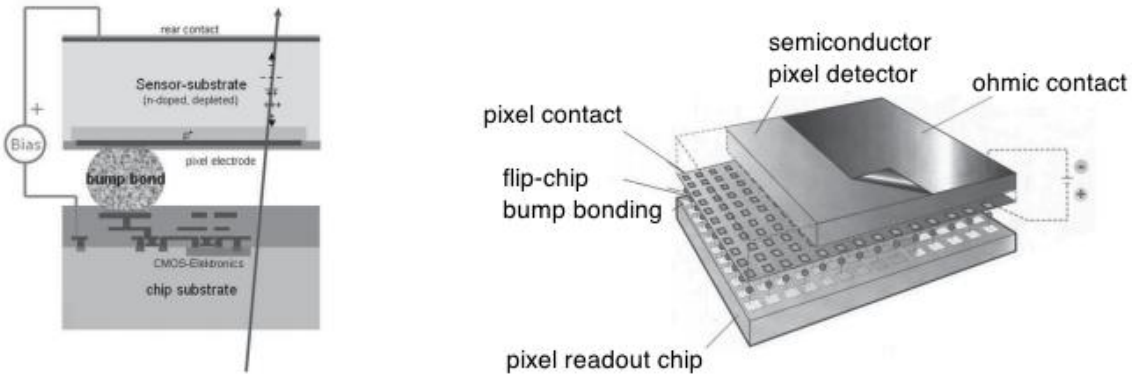

Figure 2.5: Setup of a Hybrid Pixel Detector.

is the process of inserting atoms that either have an additional valence electron (donor, n doping) in comparison to the atoms of the material or have one fewer valence electron (acceptor, p doping). The donors provide additional states close to the conduction band. Acceptors provide additional free states close to the valence band.

For silicon detectors a combination of n-type and p-type silicon is used. When the p- and n-type silicon meet the different charge carriers (electrons and holes) diffuse towards the oppositely doped side and recombine. A depletion region with no free charge carriers grows but an electric field is induced by the remaining space charges, acting against the diffusion and providing an equilibrium for a particular width of the depletion zone. The width of the depletion zone can be increased further by applying an external voltage, called a bias voltage. To use the complete sensor one needs to extend the depletion zone across the whole of the detector because the signal increases with the width of the depletion zone. Only the electron-hole pairs produced in the depletion zone contribute to the signal as only there they can drift due to the electric field. In the non-depleted region the pairs are not separated by the field and hence recombine very quickly. If the applied voltage is too high a junction breakdown can occur. This increases the noise in the read-out electronics by increasing the so-called leakage current.

Setup of a Hybrid Pixel Detector

When a charged particle moves through a semiconducting material it leaves electron-hole pairs along its track. If a field is applied on the sides of the semiconductor the charge carriers drift towards the electrodes whilst inducing a signal.

Pixel detectors allow for a 3D resolution of a particle track. To provide a quick signal readout the most commonly used setup is a hybrid pixel detector, where the sensor and the readout are located in different pieces of silicon [7]. While the sensors are preferably

built out of high ohmic silicon, the readout is usually comprised of low ohmic silicon. The hybrid setup allows for the two different parts to be optimised individually for their respective use. Furthermore, the detector does not have to be constructed in one single laboratory, making the production process easier.

Currently, hybrid pixel detectors also provide the fastest possible signal readout, an important factor in the choice of pixel detector considering the high rate of collisions happening at the LHC. Every sensor is connected to their respective readout chip by a bump bond (as shown in Fig. 2.5), a technique also used in commercial applications such as CPUs. Because each pixel is read out individually, the signal can be acquired and transmitted quickly. Monolithic sensors, which only consist of one piece of silicon, are not currently built to read out each pixel individually, instead reading out one pixel after the other, making it much more likely to miss hits if particles pass through the detector at a high rate.

For these reasons, hybrid pixel detectors are the most commonly used pixel detectors in high energy physics experiments. Additionally, the pixel detector readout allows for pixels to be clustered together, e.g. multiple adjacent pixels can register a signal and are hence likely to belong to the same signal. This can decrease the amount of data that needs to be stored.

2.3.2 Diamond Pixel Detectors

Silicon is the most accessible material to build pixel detectors, but has its limitations. As the pixel detector is the closest detector to the collision point, the high flux of particles can damage the sensors and render them useless after prolonged use. As the ATLAS collaboration is currently preparing for the upgrade of the detector for the high luminosity LHC (HL-LHC), it is important to find solutions for more resistant detectors.

One of the options currently considered is the use of diamond as a sensor material. Diamond is very radiation resistant with a displacement energy of 42 eV/atom [9] but the signal will be smaller, due to the larger band gap in diamond (5.48 eV) compared to that of silicon (1.12 eV) [8]. Equally, the noise level will be smaller. It was calculated, that for high particle fluences the signal to noise ratio in diamond will be larger than for silicon [10], which makes it a promising candidate for the ATLAS upgrade.

Diamond pixel detectors can be constructed in different setups. They can be built in a planar geometry, with electrodes at the top and bottom of the sensor. Another possibility is incorporating the electrodes into the sensor material, as shown in Fig. 2.6. Diamond has a large number of traps, similar to irradiated silicon. If an electric field is applied the charge carriers move more quickly, reducing trapping probability. If the distance travelled

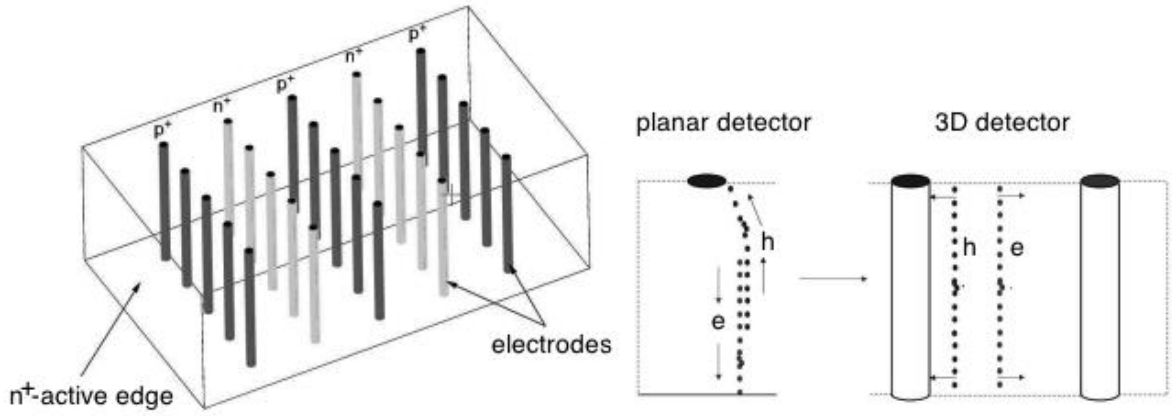

Figure 2.6: Schematic setup of a 3D diamond pixel detector in comparison to a planar detector.

by the charges becomes smaller, the trapping probability also decreases. This means the signal measured in 3D diamond detectors is larger than the signal measured in detectors of the same thickness with planar geometry, which is why 3D diamond is currently the preferred option for new pixel sensors.

Diamond sensors are not depleted. Due to the large band gap, there are not many thermally generated electrons and holes at room temperature. The applied electric field is used to separate the charge carriers and in a 3D sensor the electrodes are closer together, so the charge collection time is shorter. Equally, this means that the applied voltage in a 3D geometry can be lower to create an electric field which has the same strength as the one in a planar sensor.

3 Experimental Setup

3.1 The FE-I4 Readout Chip

The readout chip that is used to process the signal of the sensors is the Front-End I4 (FE-I4) integrated circuit [11]. It contains the readout electronics for 26800 hybrid pixels. The chip consists of 80 columns and 336 rows, with the pixels each having a size of 250 μm $\times$ 50 μm.

A particle travelling through the sensor leaves a track of electrons and holes, which move towards the electrodes due to the applied electric field. The instantaneous induced current i_k on the electrode can be calculated according to Ramo's theorem [12]:

$$i_k = q\vec{v}\vec{E_W} \tag{3.1}$$

with $\vec{v}$ being the drift velocity of the charges, q the total deposited charge and E_W the weighting field, which can be derived from the voltage at the electrodes and the geometrical configuration. The total charge can then be determined by integrating the induced current over time. Experimentally that can be achieved with a charge sensitive amplifier, which consists of an operational amplifier with a capacitor in the feedback, illustrated in Fig. 3.1. The capacitor is then discharged by a constant current. This leads to a triangular pulse. As the next step, a discriminator compares the pulse to a set threshold. If the signal is above the threshold, then the output is a logical one, and zero otherwise. The time for which the output is not zero (time-over-threshold, ToT), is proportional to the induced charge. These readout electronics are contained in each pixel of the FE-I4 chip.

The signal from the FE-I4 chip is then transmitted to an MMC3 board (see Fig. 3.2), which is the hardware for the USB-based readout system for the FE-I3 and FE-I4 sensors, USBpix. The corresponding graphical user interface is STControl, which is based on ROOT and Qt and allows to easily configure the sensor and perform different scans.

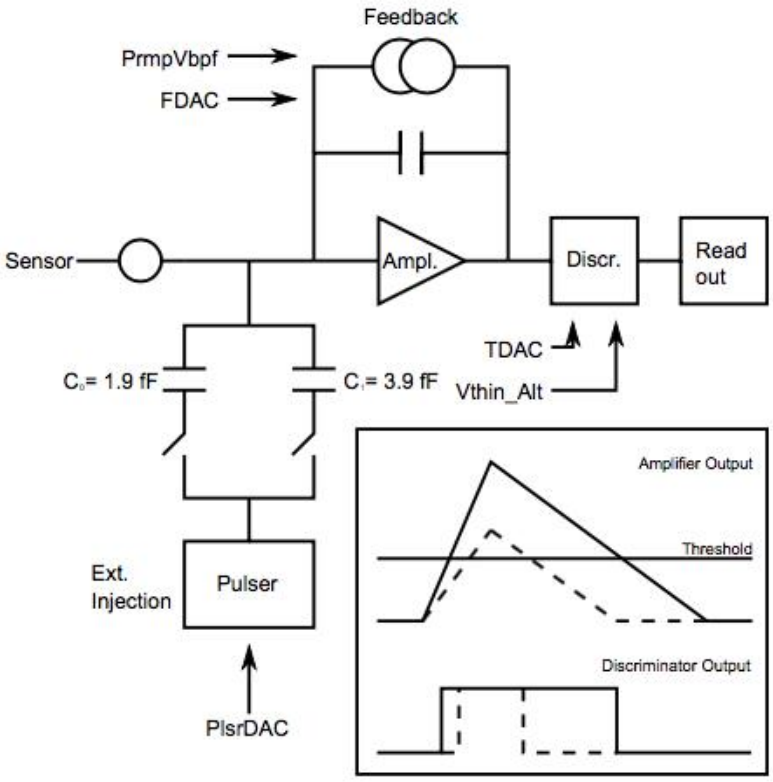

Figure 3.1: Readout Electronics of a Hybrid Pixel Detector.

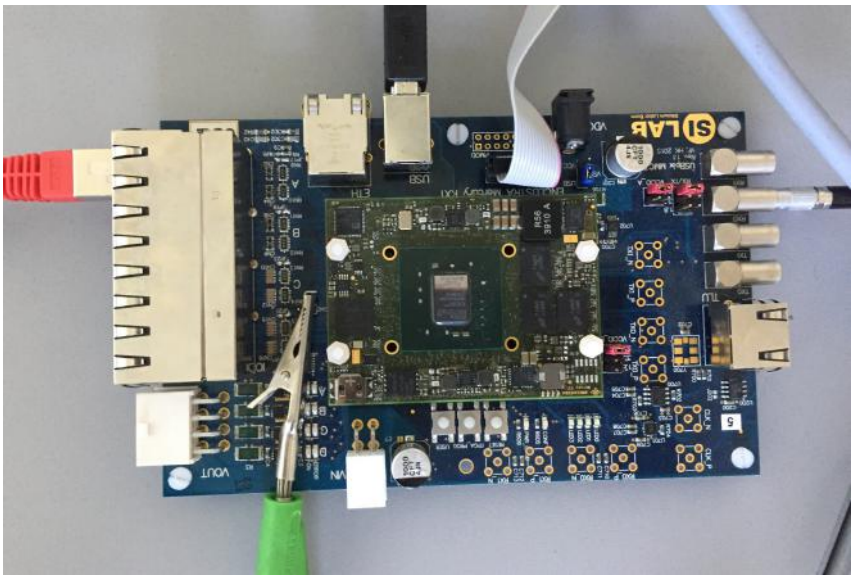

Figure 3.2: The MMC3 board.

3.2 Standard Scans

To understand the behaviour of modules it is important to characterise the Front-End electronics and to calibrate and tune the chip. In the following, some standard scans are described, which are already implemented in STControl and serve as a basis for the new tuning.

Digital Test and Analog Test

The FE-I4 allows for a charge to be injected in each pixel, either in the discriminator (Digital Test) or amplifier (Analog Test). The injection is done multiple times and the number of events observed in each pixel is counted, providing a measure for how well the analog and digital components of the FE-I4 work. In an ideal module, all of the pixels should show the same number of hits, which should equal the injected charge. Any discrepancies from this result are results of malfunctioning or noisy pixels. The analog and digital test provide a good first impression of the quality and possibly particular features of the module. For this reason, these two scans are usually the first steps in the tuning procedure.

Charge Injection Calibration

As the next step of the tuning, the charge injection mechanism is calibrated. The charge is injected using a pulser and two capacitors, which can be connected individually or in parallel. Based on simulations of the chip layout, the capacitances are expected to be $C_0 = 1.8$ fF, $C_1 = 3.9$ fF and $C_{\text{comb}} = 5.85$ fF, but the true values can differ in each pixel. The voltage step, which is applied to the injection capacitor is controlled by the `PlsrDac` value, which relates the injected charge to the capacitances, the conversion factor V_{Grad} and the calibration offset V_{Offset}:

$$Q_{\text{inj}} = C_{\text{inj}}(\texttt{PlsrDac} \cdot V_{\text{Grad}} + V_{\text{offset}}) \tag{3.2}$$

The aim of the `PlsrDAC` calibration is to find the values of V_{Grad} and V_{Offset}. To find V_{Grad} a DAC Scan is performed. The scan measures the voltage applied for different `PlsrDac` values. It mostly shows a linear behaviour as shown in Fig. 3.3, which is also what would be expected from Eq. 3.2. Injection into different numbers of columns at the same time can be chosen by the `Colpr_Mode` variable, with the possible values described in Tab. 3.1 and the different settings show a different saturation behaviour.

Colpr_Mode	Action
0	Only the addressed double-column is scanned
1	Every fourth double-column is scanned
2	Every eighth double-column is scanned
3	Every double-column is scanned

Table 3.1: Parameters for the PlsrDAC measurement.

The saturation occurs earlier if more double columns are selected for injection, because this decreases the available PlsrDAC current. The DAC Scan returns a value for the gradient, which was measured to be around 1.5 mV per DAC step, which is equal to approximately 55 e/DAC step.

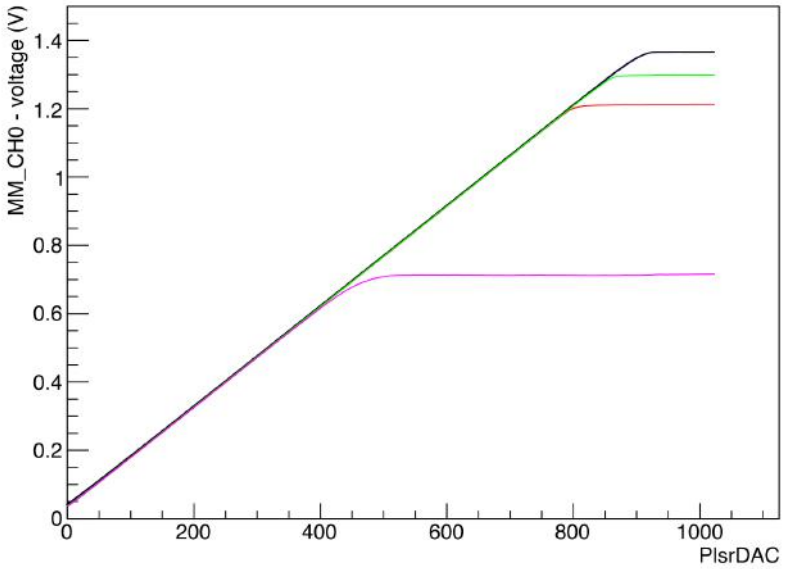

Figure 3.3: Example for the PlsrDAC calibration. The colours of the lines correspond to the different Colpr_Mode settings with: black - Colpr_Mode=0; green - Colpr_Mode=1; red - Colpr_Mode=2; pink - Colpr_Mode=3.

To determine the offset of the PlsrDAC an Injection Calibration Scan can be performed. This scan consists of three Threshold Scans, which are described in the following section, where each scan is done with one of the three different injection capacitances C_0, C_1 and C_{comb}. The combination of the three measurements allows the offset to be determined very precisely. Depending on the chip, the offset value was observed to be in the range of $10 - 20$ mV, which corresponds to a charge of $370 - 740$ e.

Threshold Scan

One important variable of the FE chip is the discriminator threshold. To verify this value, a threshold scan can be performed, which measures the occupancy of a pixel as a function of the injected charge. Ideally, this distribution should be a step function, but due to noise effects the distribution is smeared out and forms a so-called S-curve, that can be seen in Fig. 3.4.

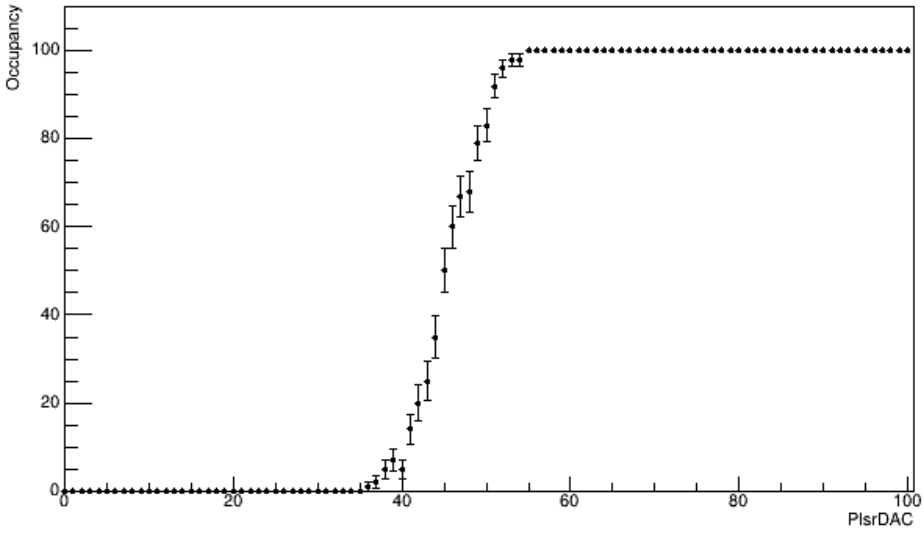

Figure 3.4: Result of a threshold scan.

The S-curve can be described by an error function:

$$p_{\text{hit}} = \frac{1}{2}\text{Erfc}\left(\frac{q_{\text{thresh}} - q}{\sqrt{2}\sigma_{\text{noise}}}\right) \tag{3.3}$$

where p_{hit} is the hit probability, q_{thresh} is the threshold charge, q is the injected charge and σ_{noise} is the equivalent noise charge.

Noise Occupancy

The Noise Occupancy Scan is a tool for measuring the amount of noise in a sensor. During the scan, the occupancy in the pixels is measured, without any source present. The FE triggers with a fixed frequency and counts the number of hits in each pixel. The scan provides a map of the noise occupancy, as well as a total number of pixels above a defined hit rate. This allows to identify noisy or hot pixels and disable them, if necessary.

Source Scan

To test the behaviour of the sensor in the presence of sources a source scan can be performed. The particles from the source leave electron-hole pairs in the sensor, which are measured instead of an injected charge. With, for example, a radioactive source present, the occupancy of each pixel is measured when a trigger is sent. There are multiple options for triggering in a source scan, two of which were used in the following measurements. The first one is using an external trigger, usually a function generator. This just provides a trigger signal with a particular frequency. As a consequence, not every hit is registered. This means that the external trigger is good for sources that provide a high rate of particles.

The other option is using the self trigger of the FE-I4B. With this option, the trigger is generated by the hitbus, which indicates if there has been a hit anywhere on the chip by considering the discriminator output of all pixels. For each rising edge on the hitbus a trigger is sent. But if there are too many hits the hitbus constantly stays active and there are no rising edges, so no triggers are sent. As a result, the self trigger is a better option for sources with a lower intensity.

3.3 Threshold Tuning of the FE-I4B

3.3.1 Standard Tuning

The standard tuning of the Front-End Readout chip takes place in different stages. At first, the global threshold (GDAC) is adjusted to the approximate value needed. The GDAC is saved in the module configuration using two different parameters: Vthin_AltFine and Vthin_AltCoarse, which give the GDAC according to GDAC = Vthin_AltFine + $256 \cdot$ Vthin_AltCoarse. For most measurements, including the ones in this project, Vthin_AltCoarse = 0, so GDAC and Vthin_AltFine can be used interchangeably. After the GDAC tuning, the local threshold values (TDAC) for each pixel are adjusted, to reduce the spread of the thresholds across all pixels. Finally, the feedback current (FDAC) is adjusted, which calibrates the time over threshold for a given charge. The whole tuning procedure is usually done by injecting charge directly into the preamplifier, which is shown in Fig. 3.1. However, this method produces digital activity in the sensor, for example, a capacitance in one pixel can lead to a signal being induced in a neighbouring pixel. These effects can make it difficult to reach very low thresholds.

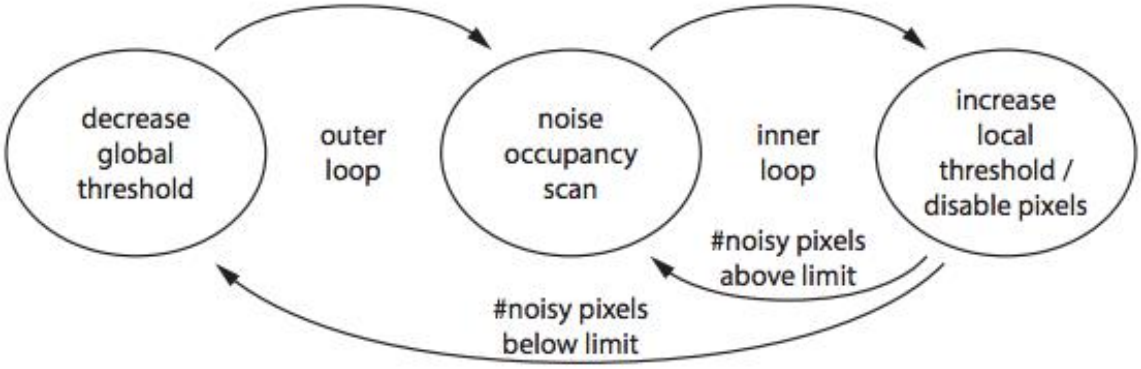

Figure 3.5: An illustration of the Threshold Baseline Tuning algorithm.

3.3.2 Threshold Baseline Tuning

Diamond sensors are a promising option for future pixel detectors, but they produce a smaller signal, due to their larger band gap. Hence for a use in ATLAS, the correct tuning of the threshold becomes much more important. For silicon detectors the threshold can usually be set to a high level above the noise but for diamond it is desirable to lower the threshold as close as possible to the noise level. To achieve this, a new threshold tuning method has been developed [9], which now has to be implemented into the standard software of the sensor.

The Threshold Baseline Tuning algorithm does not require an external injection of charges. Instead, it measures the noise hit rate of each pixel and sets the individual thresholds accordingly. The algorithm is illustrated in Fig. 3.5.

At first, the GDAC is set to a high value and the TDAC is set to the highest value possible. A high TDAC equals a low threshold and a decrease in TDAC is equal to an increase in threshold. A noise occupancy scan is then performed and if pixels show an excess of noise hits, their TDAC is decreased. The noise occupancy scan and increase of the local threshold for noisy pixels is then repeated until the total number of noisy pixels (NoisyPix) is below a certain limit (inner loop). The local threshold is then kept constant whilst the global threshold is decreased (outer loop). If the upper limit of the local threshold for a pixel is reached, the pixel is disabled. The outer loop stops if the number of disabled pixels (DixPix) is above a certain chosen limit. The algorithm and the reached thresholds are controlled by the two parameters NoisyPix and DixPix.

4 Measurements

4.1 Implementing the Threshold Baseline Tuning Algorithm

The Threshold Baseline Tuning was implemented into the standard pixel testing software STcontrol, based on the existing scans. As an inner loop a charge injection scan was used at first, similar to the standard tuning, but with the charge set to zero. According to the algorithm described above, the TDAC value of the pixel was decreased when it had an occupancy larger than zero. Additionally, the outer loop, which decreases the GDAC, was implemented and the loops and the algorithm exit according to the chosen parameters NoisyPix and DisPix.

4.1.1 Results of the Noise Occupancy Implementation

As a next step, the algorithm was tested with the particular aim of adjusting the parameters of the tuning. Firstly, the GDAC step size was a possible variable. To reduce the time needed for the tuning, the GDAC was chosen to decrease in steps of 2, increments still small enough for the algorithm to converge. The most important step was choosing the parameters NoisyPix and DisPix, as they defined the threshold that was to be achieved. At first, values of 100 were tried for each variable. This turned out to be approximately the number of pixels that are always noisy. This can be seen in the noise occupancy map in Fig. 4.1 in which the pixels around the edges of the chip are particularly noisy for the specific module used in the validation. To reach the noise floor of the chip both variables had to be increased, and it was observed that 500-600 was an appropriate choice for both variables. As can be seen in Fig. 4.3, the TDAC values in the pixels were changed without any particular pattern, an indication that the noise floor had been reached. After the tuning is performed the remaining noise should be of stochastic nature, which is what is seen in the noise occupancy map after the tuning in Fig. 4.2. Unless otherwise stated, the module used for the following scans was an FE-I4B chip with a thickness of 100 μm, which is known to suffer from problems with the under-bump metallisation. This explains the

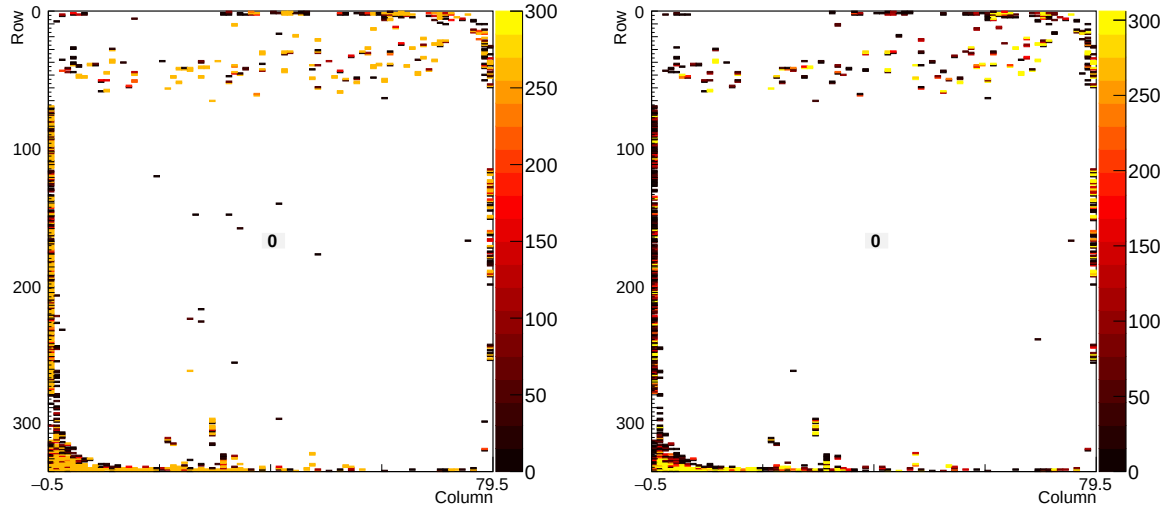

(a) Occupany before tuning, measured with a noise occupancy scan.

(b) Occupancy before tuning, measured with a source scan.

Figure 4.1: Occupancy before tuning measured with the two different implementations.

rather high noise and the peculiar pattern of noisy pixels along the edges of the module.

To get a first estimate of the threshold, a threshold scan can be performed. By fitting a Gaussian to the threshold distribution, the average threshold was found to be 788 e, with a spread of 323 e. This measurement cannot be treated as being precise, as there are multiple effects that can affect the result of a threshold scan. In particular, there is an offset introduced by PlsrDAC calibration that cannot be easily determined. A more precise measurement of the threshold reached and the offset value is described in section 4.2.

4.1.2 Source Scan Implementation

Even though the implementation described above works, there is an issue with the measurement of the occupancy in the inner loop. So far, the charge injection mechanism with an injected charge of zero has been used. This still means that the electronics related to the charge injection mechanism were switched on, potentially introducing unnecessary noise in the pixels. A better solution is to use a source scan without a source present, which does not require the charge injection components to be switched on. A function

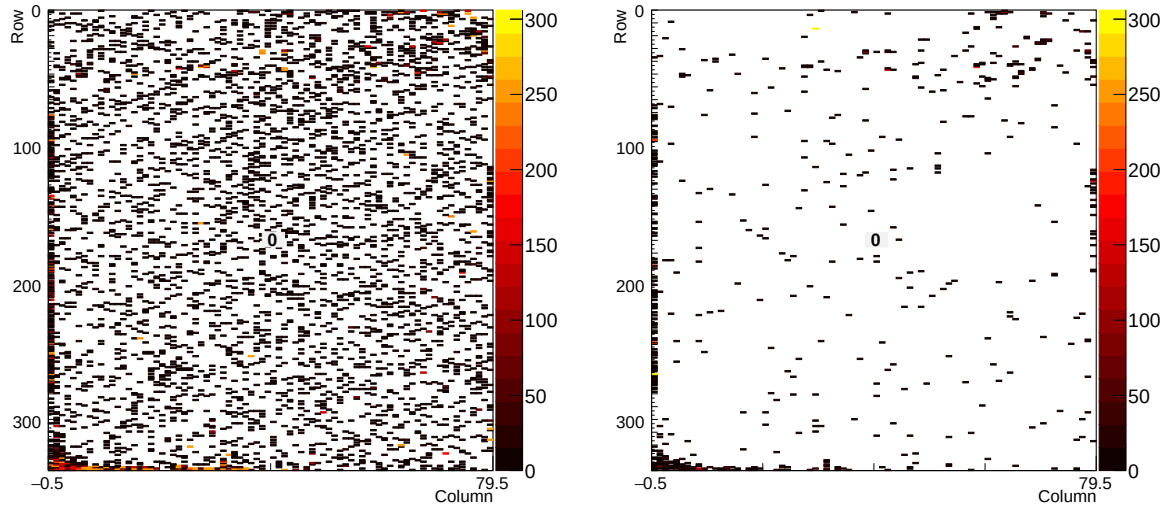

(a) Occupany after tuning, measured with a noise occupancy scan.

(b) Occupany after tuning, measured with a source scan.

Figure 4.2: Occupancy after tuning measured with the two different implementations.

generator provides an external trigger. Due to the fast external trigger and without having to turn on the charge injection circuit, the source scan implementation reduced the time needed for tuning by approximately a factor of 2.

For the implementation of the algorithm, the inner loop was changed from a noise occupancy scan to a source scan while the remaining code stayed the same. A source scan without a source returns a very similar result to a noise occupancy scan at high thresholds and shows the same noisy pixels as can be seen in Fig. 4.1. This observation supports the decision to choose the parameters NoisyPix and DisPix to be the same as those for the noise occupancy implementation. The source scan tuning leads to a similar TDAC distribution as the noise occupancy tuning, as can be seen in Fig. 4.3. When the tuning was performed, the algorithms stopped at GDAC=102 if the noise occupancy tuning was used with DisPix=600 and NoisyPix=600. For the source scan tuning the tuning stops at GDAC=72 when using the same exit conditions, a very unexpected observation. A small difference in the final GDAC was expected due to the smaller noise effect for source scan tuning. As can be seen in Fig. 4.4, a difference of 30 GDAC steps can be equal to a difference in threshold of around 1000 e, especially for low thresholds. An offset is expected in the PlsrDAC value, which would also be observed if the injected charge was

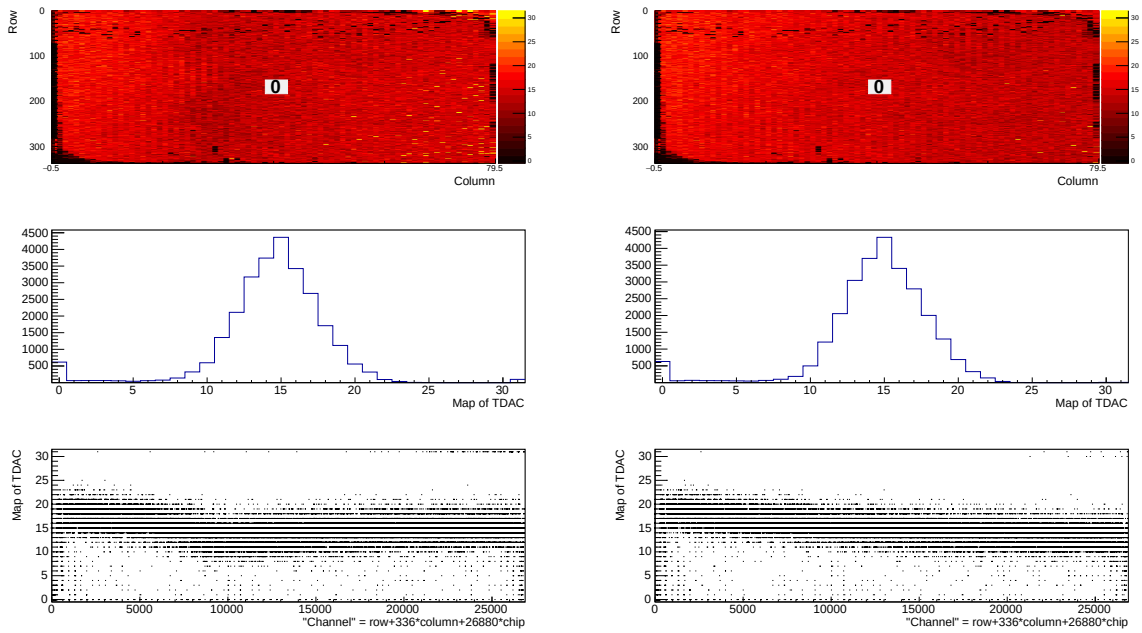

(a) TDAC distribution after noise occupancy tuning.

(b) TDAC distribution after source scan tuning.

Figure 4.3: TDAC distribution after tuning with noise occupancy and source scan implementation. A map of TDAC values is shown at the top, a distribution of TDAC values for all pixels is shown in the middle and a scatter plot of TDAC values for each pixel at the bottom.

zero. However, this offset was expected to be in the order of magnitude of 100 e. The observed value is much higher than previously expected and this offset requires further investigation. To get a more accurate measurement of the offset, measurements with different sources were performed later and described in section 4.2.

4.1.3 Comparison to Standard Tuning

The standard tuning and Threshold Baseline Tuning are based on entirely different mechanisms. Nevertheless, it is interesting to compare the different tuning results. Firstly, the standard tuning, consisting of GDAC, TDAC and FDAC tuning, is only possible for relatively high thresholds above 2000 e, due to the uncertainty in the charge injection. Lower thresholds can only be reached with successive TDAC adjustements and the tuning becomes less precise. A positive feature however, is that the standard tuning allows a particular threshold to be chosen as a tuning point, whereas the Threshold Baseline Tuning only allows the choice of the exit conditions and a measurement of the reached threshold is

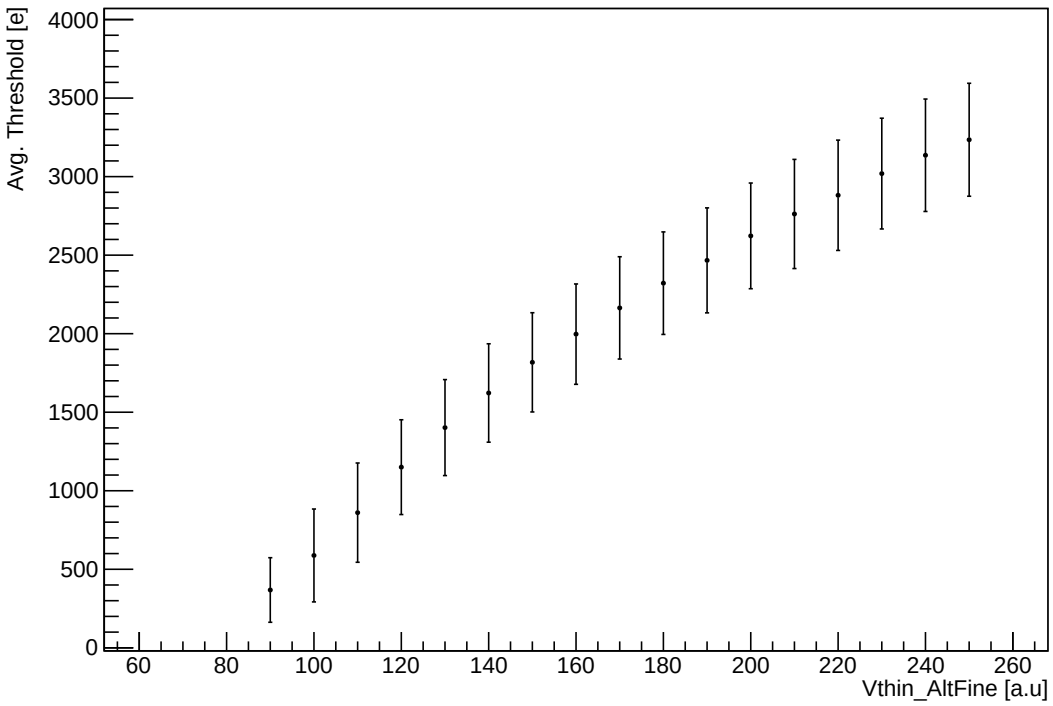

Figure 4.4: Measurement of the threshold as a function of Vthin_AltFine for the Threshold Baseline Tuning. The errorbars represent the spread of the threshold distribution over all pixels.

not trivial. This is the case because, as described above, the threshold scan stops working for low thresholds and especially for these thresholds the offset becomes very relevant, so it has to be measured beforehand. But a major advantage of the Threshold Baseline Tuning can be seen when comparing the TDAC maps of the two tuning algorithms in Fig. 4.5. The Threshold Baseline Tuning was done with the usual parameters NoisyPix=600 and DisPix=600. The standard tuning procedure was done for a desired threshold of 3000 e. The achieved threshold is obviously different, but the TDAC distribution is usually adjusted around the actual threshold, making it a useful quantity to compare. As can be seen in Fig. 4.5, the histogram of the different TDAC values looks very similar for both tuning methods but the distribution of the TDAC values across the pixels is different. For the Threshold Baseline Tuning, the low TDAC values are found at the pixels that were particularly noisy before, which can be seen when comparing the TDAC map to the noise occupancy scan in Fig. 4.1. This is the desired effect, as a low TDAC equates to a higher threshold, leading to the noisy pixels effectively being masked. On the other hand,

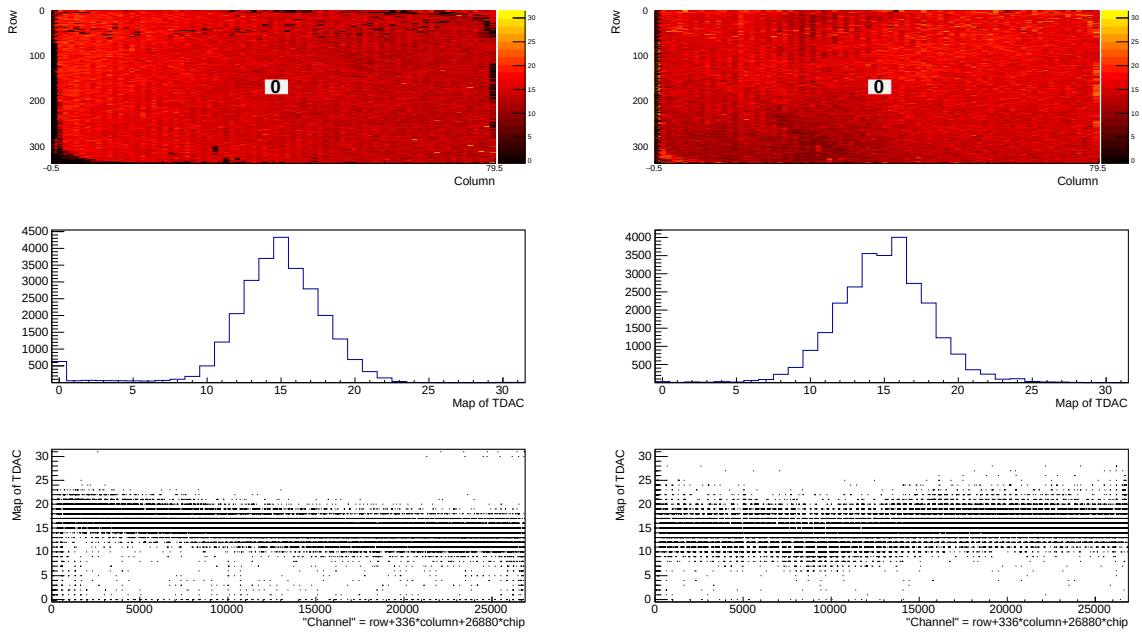

(a) TDAC map after Threshold Baseline Tuning.

(b) TDAC map after standard tuning.

Figure 4.5: TDAC maps for tuning with Threshold Baseline Tuning and the standard tuning procedure. A map of TDAC values is shown at the top, a distribution of TDAC values for all pixels is shown in the middle and a scatter plot of TDAC values for each pixel at the bottom.

the TDAC map for the standard tuning does not show this particular pattern, instead the TDAC values seem to be fairly evenly distributed over the entire module. From this comparison it can be seen that the Threshold Baseline Tuning has the desired effect, adjusting the more noisy pixels such that they will register fewer or zero noise hits. This property may be particularly helpful when considering irradiated modules. The affected pixels could be adjusted without necessarily increasing the threshold of the entire module, leading to a better signal and longer possible use.

Another aspect worth comparing between the two algorithms is the threshold distribution. A threshold scan at the final tuning point of the baseline tuning is impossible, due to the offset from the charge injection mechanism. However, the tuned threshold distribution can be shifted to higher values without significantly changing the shape of the distribution. This can be done by manually adjusting the GDAC in the configuration of the module. In fact, this is one of the main components of the source measurements described in section 4.2. The results for the standard tuning and the shifted baseline tuning can be seen in Fig. 4.6. It can be seen that the shapes show different characteristics.

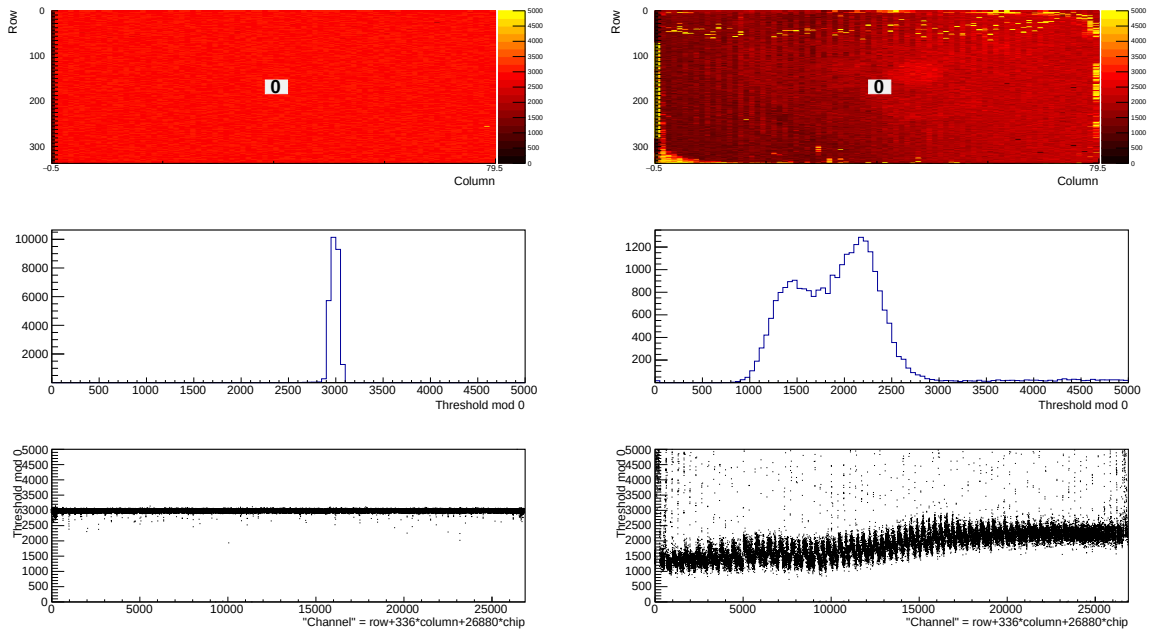

(a) Threshold scan for standard tuning to 3000e.

(b) Threshold scan for baseline tuning with NoisyPix=600 and DisPix=600, shifted to GDAC=150.

Figure 4.6: Threshold scans for standard and baseline tuning. A map of the threshold values across the module is shown at the top, the distribution of thresholds for the module is shown in the middle and a scatter plot of the threshold value for each pixel at the bottom.

The standard tuning produces a fairly narrow distribution, in this case with a spread of 200 e. The distribution appears symmetric with a peak around a particular value. This shape is due to the fact that the tuning focuses on tuning every pixel to a particular threshold given in electrons and the spread of the thresholds is only due to the fact that the TDAC steps are not equal for each pixel and thus not all pixels are able to reach the desired threshold equally well. The baseline tuning, on the other hand, leads to a much broader distribution with a spread of around 500 e. Furthermore, the shape does not resemble a Gaussian. The shape has this appearance as the threshold in a particular pixel is only dependent on the noise in that particular pixel. This noise can vary for different pixels, leading to a wider distribution as no tuning goal is set. The threshold map also reproduces the pattern of noisy pixels around the edges of the module, which have been observed in the TDAC map and the noise occupancy scan previously and are now set to high threshold values.

4.2 Testing the Threshold Baseline Tuning Algorithm

The Threshold Baseline Tuning allows to reach very low thresholds close to the noise floor, especially when using the source scan implementation. At these thresholds the standard threshold scans stop working. In particular, there was an offset observed in measurements that used the charge injection mechanism, including threshold and noise occupancy scans, in comparison to those that did not, as described in section 4.1.2. This implies that the thresholds achieved by the standard tuning are higher than the threshold scans indicate. This offset was found to be of the order of magnitude of 1000 e, and so it may not be a significant problem in the current data taking, as the signal of the particles is much higher than the usual threshold. When it comes to detector development however, the offset is a factor that needs to be considered, particularly when working with materials that produce lower signals, such as diamond. Generally, when using these materials and tuning with the Threshold Baseline Tuning algorithm, it is important to have a good understanding of the threshold reached, as well as its distribution. This also implies a precise knowledge of the offset. For this reason, the main goal of the measurements was to find the value of the offset by employing different methods and sources with a variety of energies in order to obtain independent measurements and to study the energy dependence of the offset value.

4.2.1 X-ray Measurements

To verify the Threshold Baseline Tuning sources which deposit little energy in the sensor are desirable, since the tuned threshold is very low. Usually, source measurements are done with a radioactive source, but none of the available sources have an energy peak below 3000 e, which is the region that is particularly interesting. Additionally, the absorbed energy has to be known accurately, leading to the choice of a source that emits photons. Photons are completely absorbed within the sensor, allowing the energy of the photons to be easily reconstructed from the number of produced charge carriers. This reasoning provided the motivation to try a different type of source measurement, using X-ray tubes instead of radioactive sources, in which the spectra possess characteristic lines at low energies. Three different materials were used for the X-ray anode: Iron, Copper and Molybdenum. An overview of the energies for the characteristic lines of different materials can be found in Tab. 4.1, with their respective number of produced electrons as the radiation is absorbed, and relative intensity, with 100 as the maximum. The number of produced electrons can be calculated by dividing the energy by 3.6 eV, the average energy needed to produce an electron-hole pair in silicon [8].

Material	Energy [eV]	Number of e	Rel. Intensity
Fe	6390.8	1775	50
	6403.8	1779	100
	7058.0	1961	17
Cu	8027.8	2230	51
	8047.8	2236	100
	8905.3	2474	17
Mo	17374	4826	52
	17479	4855	100
	19590	5442	8
	19608	5447	15
	19965	5546	3

Table 4.1: Energies and equivalent charges for different X-ray sources. The values are taken from the X-ray tube manual.

In particular, the Cu and Fe lines exist in an interesting range of energies, around 2000 e. The Mo lines can be used to check if the offset depends on the energy of the source and the offset. The experimental setup can be seen in Fig. 4.7. The sensor was positioned in front of the aperture of the X-ray source and connected to the usual power supplies, high and low voltage. The readout was processed by a USBpix MMC3 board that was connected to the sensor via an ethernet cable. Additionally, a function generator with a square wave voltage at 10 kHz acted as an external trigger and was connected to the USBpix board.

The general principle of the measurement was to measure the occupancy of different pixels as a function of GDAC. The GDAC and thus the threshold was increased, whilst the TDAC values of the pixel were kept constant. The X-ray tube provided an X-ray spectrum which could be measured as a function of angle using Bragg diffraction. The resultant spectrum can be converted into an energy spectrum which then leads to a spectrum as a function of produced charge carriers, which is shown in Fig. 4.8 for a copper anode. When measuring the occupancy of a pixel using the source scan, the occupancy should be the integral of the spectrum above the threshold. However, due to noise in the S-curve, this threshold will be slightly smeared, a factor that needs to be taken into account in the analysis. Using a measured spectrum, the spread of the S-curve and the thresholds over the pixels, the development of the occupancy as a function of threshold can be predicted, the result of which is shown in Fig. 4.8. In the prediction the equivalent noise charge and thus the width of the S-curve is set to be 200 e, the approximate value that is usually observed. In the actual data fitting the spread will remain a free parameter, as the noise does not only depend on the spread of the S-curve, but also on the width of the

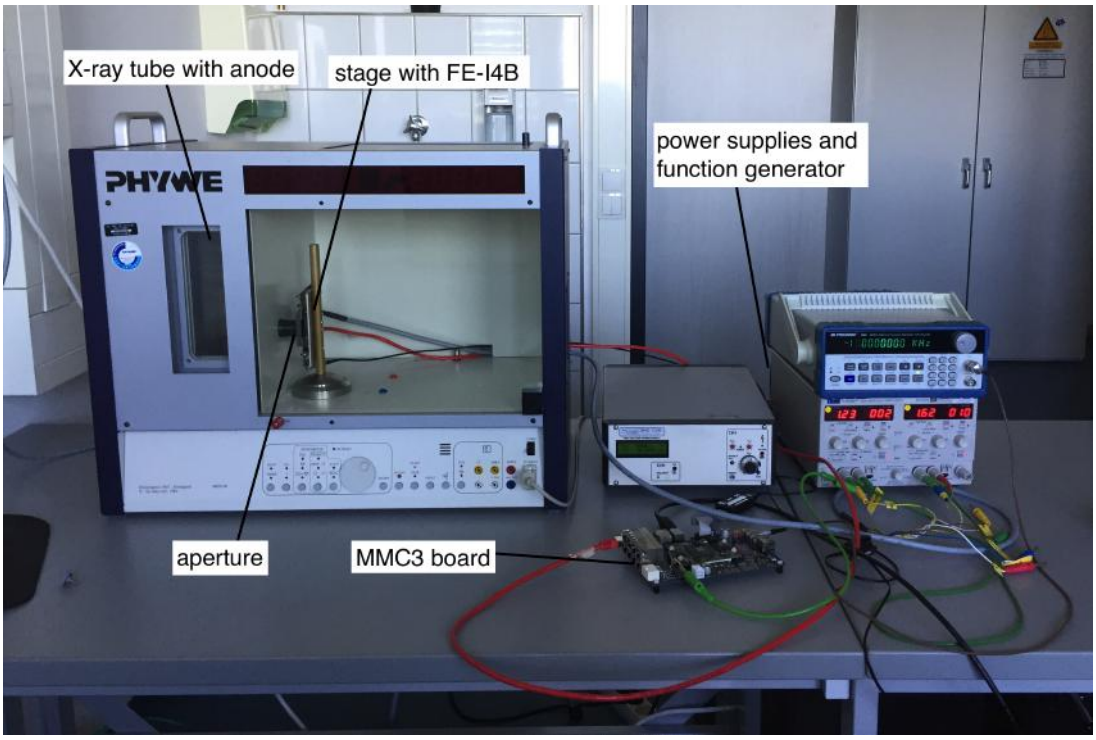

Figure 4.7: Experimental setup with the X-ray tube.

characteristic lines and possibly other noise effects. Furthermore, for the data fitting, the spectrum measured via Bragg diffraction is not the most precise data that could be used. Bragg diffraction can be described by the formula $n\lambda = 2d\sin(\theta)$, where n is the order of the maximum, λ the wavelength, d is the distance between two planes of the used crystal and θ is the angle of the incoming wave with respect to the orientation of the crystal.

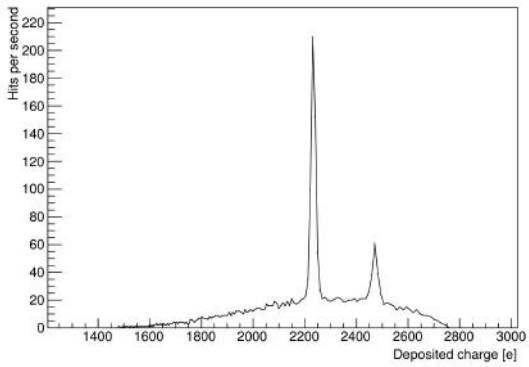

(a) X-ray spectrum of copper with an acceleration voltage of 10kV as a function of deposited charge carriers.

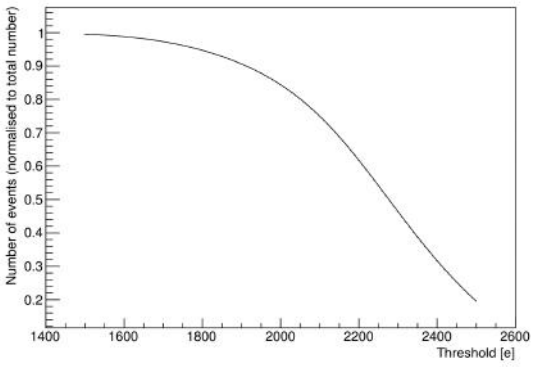

(b) Predicted relative occupancy as function of the threshold of the sensor.

Figure 4.8: Measured X-ray spectrum and derived prediction of the measurement.

Because an angular measurement of the diffraction pattern was performed, there is superposition of first, second and sometimes third order diffraction when going to higher angles, as can be seen in Fig. 4.9 for two orders. This can particularly be seen at higher acceleration voltages for the X-ray tube, increasing the total intensity. These higher order effects add to the number of hits, especially affecting the number of hits for a low number of charge carriers, since the signal there is particularly small.

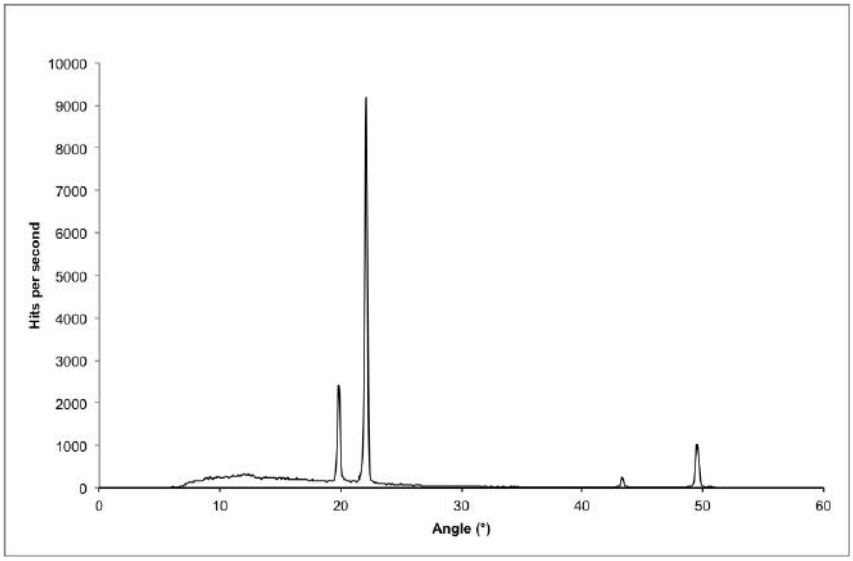

Figure 4.9: Angular measurement of the spectrum of the copper X-ray tube at 25 kV.

Reconstruction of the actual X-ray spectrum from this measurement by subtracting higher orders is not easily performed, as the amplitudes with which the signals are reflected for each angle are not known or measurable and could only be roughly estimated. This would introduce a large additional error into the prediction. Additionally, the measurement is already limited in precision by the step size of the angle and the finite time of the measurement. Instead, in order to improve the data fitting, the characteristic lines were approximated as Gaussians with their height given by their relative intensities, as shown in Tab. 4.1 and all with equal width and the same spread due to the S-curve. The spread due to the S-curve is assumed to be equal for each peak but left as a parameter for the fitting. The Bremsstrahlung spectrum is also modelled as a very broad Gaussian with the corresponding peak at the maximum of the Bremsstrahlung found in the measured spectrum. The spread of this Gaussian is also left as a free parameter in order to fit the decrease of the Bremsspectrum for low numbers of charge carriers. When comparing a Gaussian with the measured spectrum there is an expected discrepancy between the Gaussian and the distribution at higher energies, because a Gaussian does not properly represent the cut-off at the maximal energy of the spectrum, at the acceleration voltage.

However, as the most important parts of the data fitting are the data points around the energies of the characteristic lines and these are represented correctly, this approach was chosen.

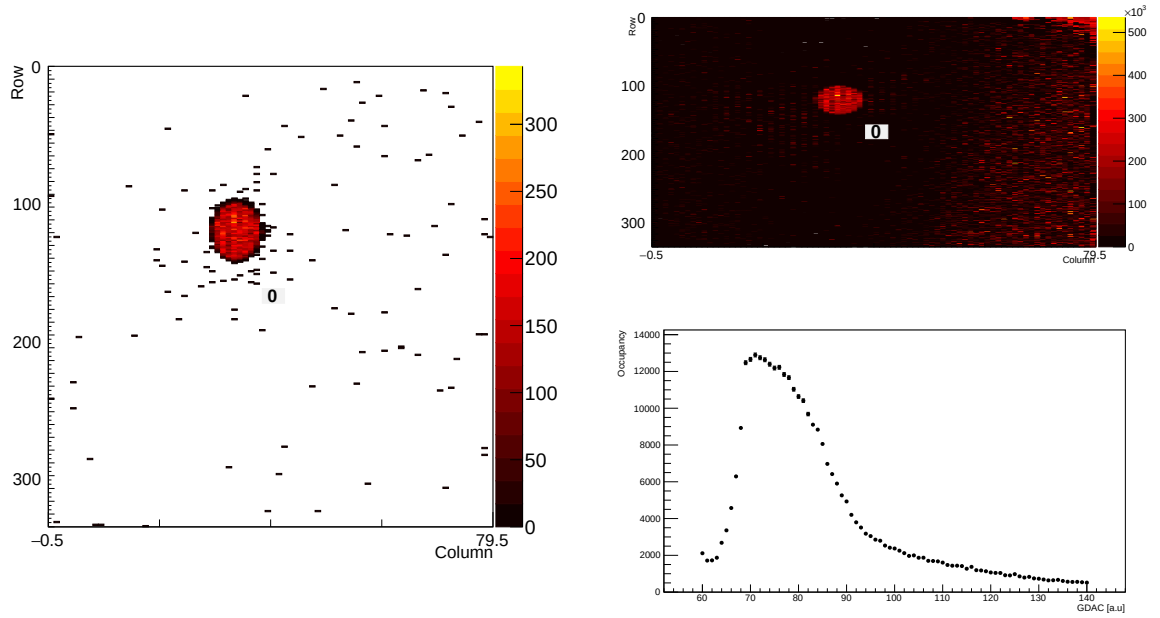

(a) Hit map for Cu at 25 kV acceleration voltage with a small aperture.

(b) Example of an occupancy against GDAC measurement. At the top a map of the occupancy is shown and at the bottom the occupancy of one particular pixel is plotted against the GDAC value.

Figure 4.10: Examples for a source scan measurement with a copper X-ray tube.

Fig. 4.10 shows two plots for a source scan performed with an external trigger set at 10kHz. The right hand side of the figure shows the occupancy of the module for a total of 100000 trigger signals with a copper anode and for an acceleration voltage of 25 kV. As can be seen, the beam is focused on a region that covers approximately 200 pixels. Since an external trigger was used, not every hit by the X-ray beam is registered, but it is also possible to see noise hits, especially around the edges, as seen before. Later on a larger aperture was used, where the region hit by the photons covers approximately 1000 pixels. In both cases it can be seen that the beam does not hit the entire sensor, and so one does not obtain a measurement of the occupancies of all of the pixels and thus not a measurement of the offset of all of the pixels. Even though the offsets may vary from pixel to pixel, e.g. due to variations in the injection capacitances, the mean should stay approximately the same, even when considering different regions of the sensor. This should be especially true when considering the central pixels of the sensors, that do not

show a particularly noisy behaviour. As a consequence, a decision was made to mostly consider the central pixels and not the ones at the edges as these are already noisy and show more hits.

Results for Copper

The first measurement of the offset was performed using a copper anode. At this stage a small aperture was used. Before the measurement was conducted, the chip was tuned using the Threshold Baseline Tuning algorithm with the tuning parameters NoisyPix=600 and DisPix=600. Then, the sensor was positioned in front of the source and the measurement of occupancy of the module against GDAC was performed using an external trigger. An example of the measurements is shown in Fig. 4.11. The measurements were first performed over the complete range of GDAC and then between GDAC=60 and GDAC=140 to highlight the particularly interesting features of the plot. The curve on the left shows a rapid decrease at around GDAC=85. This decrease corresponds to that which would be expected at the positions of the characteristic lines. Therefore, at first comparison, the data seems to reproduce the expected shape. To achieve a large number of hits, the measurements were performed with an acceleration voltage of 25 kV.

The next step is the data fitting and subsequently, the calculation of the offset. As described above, the positions and relative intensities of the characteristic lines were used to predict the spectrum. If the offset was introduced by the PlsrDAC, this would mean that for an injected charge of zero, the charge in one pixel would be not zero, but equal to the offset. When considering the Threshold to GDAC calibration, the curve would show the threshold with the offset included. The true Threshold against GDAC curve is expected to differ from this curve, shifted to the left and possibly scaled differently. For a particular known energy the true threshold to GDAC conversion can be found in two different ways.

1. The first possibility is finding the GDAC value that belongs to a particular energy. For a particular source the energy of the photons is known. Looking at the curve in Fig. 4.11 for example, the threshold is equal to the energy of the copper lines at a GDAC of around 85. This value can be found more precisely by finding the midpoint of the decrease for each pixel. Such a data point can be added into a plot with the threshold against GDAC measurement. In Fig. 4.12 the red dot represents such a data point at an arbitrary GDAC value. Now the offset is equal to the difference between the true threshold value and the measured threshold value. This difference is indicated by a blue line in Fig. 4.12.

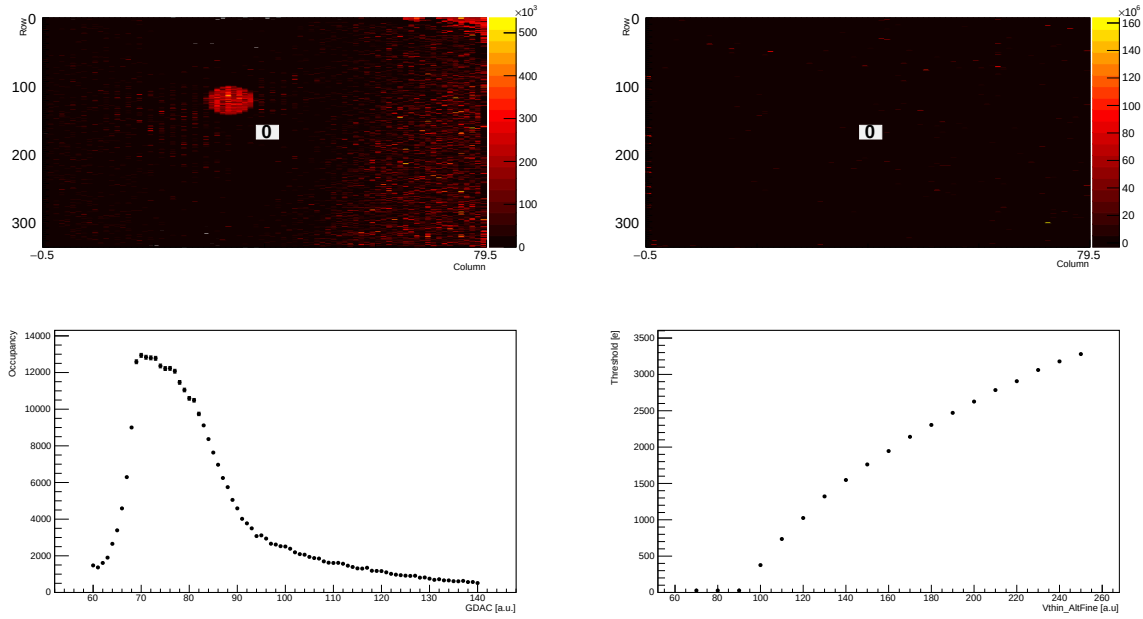

(a) Occupancy as function of GDAC for 25 kV. At the top a map of the occupancy is shown and at the bottom the occupancy of one particular pixel is plotted against the GDAC value.

(b) Threshold against GDAC for Threshold Baseline Tuning. At the top a map of the thresholds is shown and at the bottom the threshold found by the threshold scan is plotted against GDAC for one pixel.

Figure 4.11: Example of occupancy as a function of GDAC for Cu and threshold as a function of GDAC for one pixel using the Threshold Baseline Tuning.

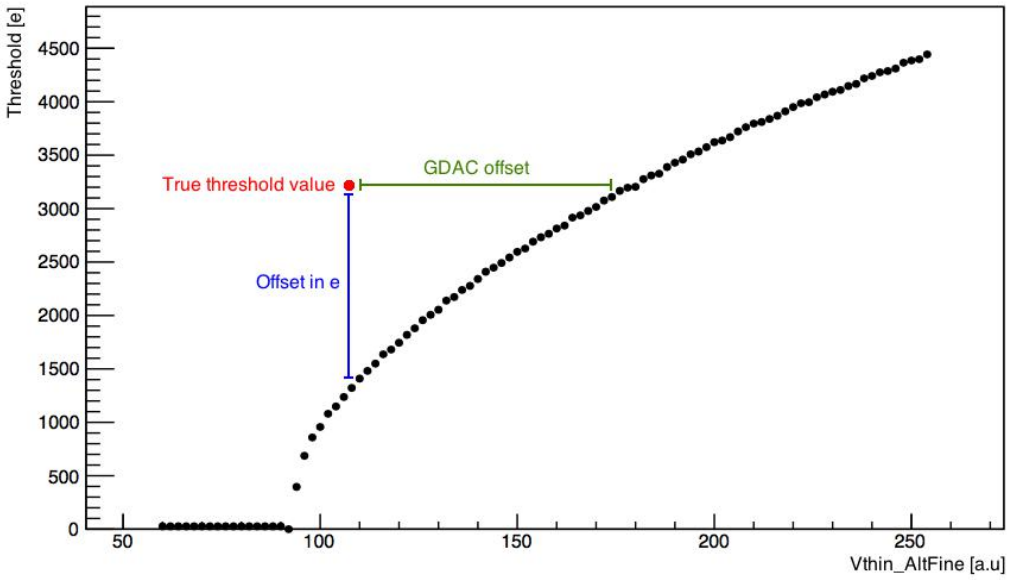

Figure 4.12: Illustration of the fitting procedure.

2. The second method involves using the measured and the predicted occupancy against GDAC. The procedure for getting the predicted occupancy against the number of charge carriers was described previously. Now the threshold against GDAC measurement can be used to convert the number of charge carriers into GDAC, which changes the shape of the curve only slightly. Compared to the measured data, the predicted curve is shifted along the x-axis by a number of GDAC steps. By fitting the prediction to the data (see Fig. 4.13) it is possible to find this shift, which is referred to as GDAC offset in Fig. 4.12. The energy of the used source is known, so one can now take the data point where the threshold corresponds to the energy of the source, according to the threshold scan, and shift it to the left by the GDAC offset. Ideally, this would return the same data point as the first method. Again, the offset in electrons can be calculated by subtracting the measured threshold value from the true threshold value. Both methods are based upon the same principles and should return the same result. There are advantages and disadvantages for both methods, depending on the quality of the data.

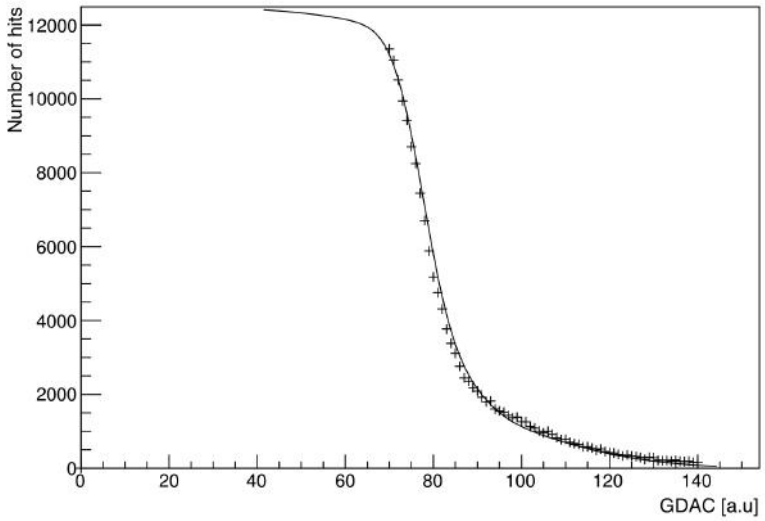

Figure 4.13: Example of the prediction fitted to the data for one pixel.

An example of the second measurement is presented in Fig. 4.14, which shows the offset for each pixel hit by the X-ray beam. The map shows the difference between the predictions and the measured data as GDAC increments. Averaging over the whole map, the average GDAC offset is (113 ± 14) GDAC units. The right hand plot in Fig. 4.11 shows that the GDAC value for the copper X-ray lines at approximately 2250 e should be at a GDAC value of approximately 180. Subtracting the GDAC offset of 113 GDAC units

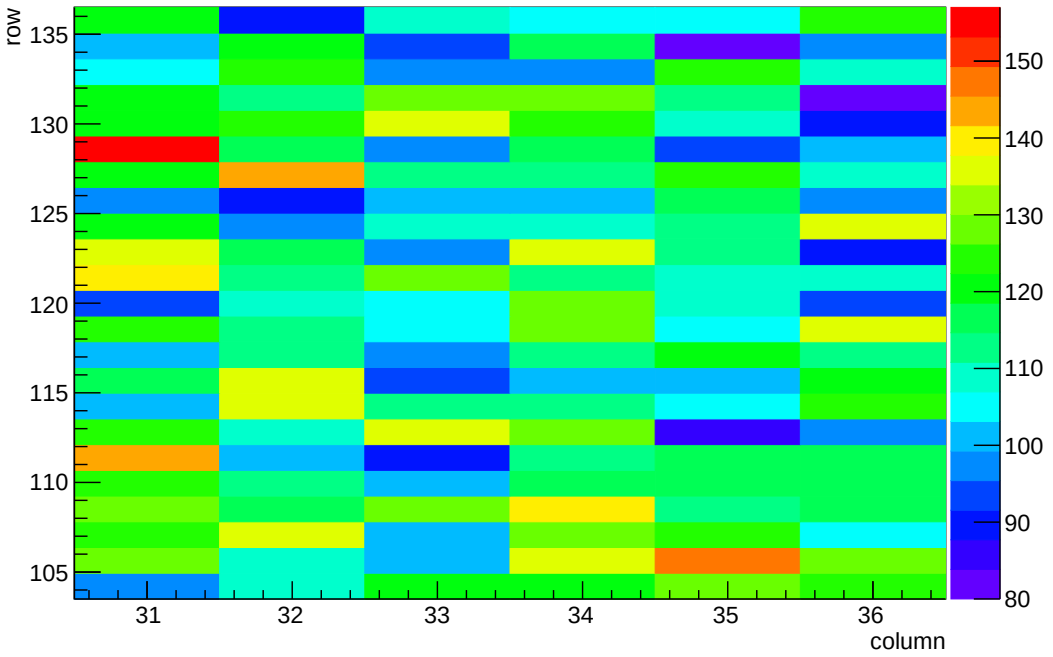

Figure 4.14: Map of the offset in GDAC for the region of interest that was hit by the beam of the Cu X-ray tube. The colours represent the GDAC offset.

implies that the threshold at 2250 e should be at a GDAC value of approximately 67. Unfortunately, threshold scans return a value of zero below a GDAC of 90. As such, it is only possible to state the number of electrons of the copper lines, approximately 2250 e, as a lower limit on the offset for this measurement.

It is also possible to attempt to find the offset using the first method, as described above, obtaining the midpoint of the decrease in the occupancy and assuming that this GDAC value corresponds to the value where the true threshold is equal to the peak of the copper X-ray line. This number of electrons can be estimated from the midpoint of the decrease in occupancy in the predictions in Fig. 4.8, that was found to be (2250 ± 50) e. One can now calculate the difference between the threshold value at the determined GDAC and 2250 e, giving the map shown in Fig. 4.15. As expected from the measurement above, most pixels show an offset of (2250 ± 50) e, again only a lower limit, as the threshold scan provides a value of zero for the required GDAC value. However, some of the pixels show values slightly below 2250 e, up to 100 e lower, which can be explained as an effect of the general spread of the offsets across the pixels. Assuming a Gaussian distribution of the offsets, this observation suggests that the actual offset is not much larger than 2250 e. Additionally, when comparing the two methods of analysis, the GDAC map and the offset

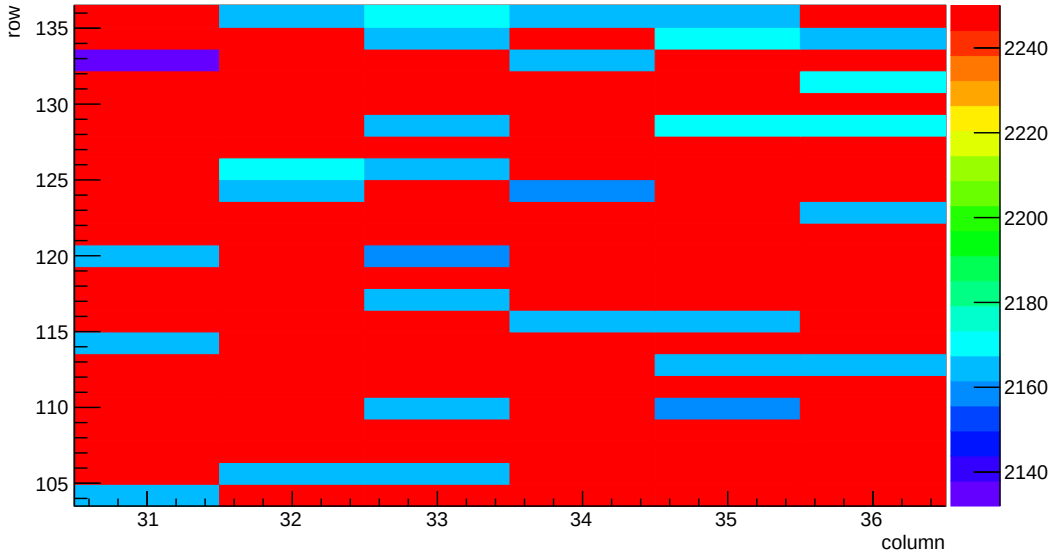

Figure 4.15: Map of the offset in electrons for the region of interest that was hit by the beam of the Cu X-ray tube. The colours represent the offset in number of electrons.

map obtained by the two different methods appear consistent, and show the same pixels having a smaller offset than the rest. As a conclusion, the measurement shows that the offset for thresholds around 2250 e has a lower limit of said 2250 e and seems to not be significantly larger.

Results for Iron

After using copper as the anode material for the X-ray tube, iron was used. Iron has lines at approximately 6390.8, 6403.8 and 7058.0 eV, which are equal to an average charge of 1780 e, even lower than that of copper. The copper measurements showed that the offset at low energies was in the order of magnitude of 2000 e, much larger than previously expected. In order to reduce possible sources of errors, especially of the ToT tuning, the standard tuning was chosen instead of the Threshold Baseline Tuning. An example of the occupancy against GDAC and threshold against GDAC measurements is shown in Fig. 4.16.

The analysis previously used to determine the offset in GDAC can be repeated, similarly to the copper measurements, leading to the map shown in Fig. 4.17. Averaging over all pixels gives a value for the GDAC offset of (90 ± 7) GDAC units. Again, this offset was subtracted from the GDAC value where the Fe lines are expected to be from the threshold scans. The difference between expected and measured values of the threshold

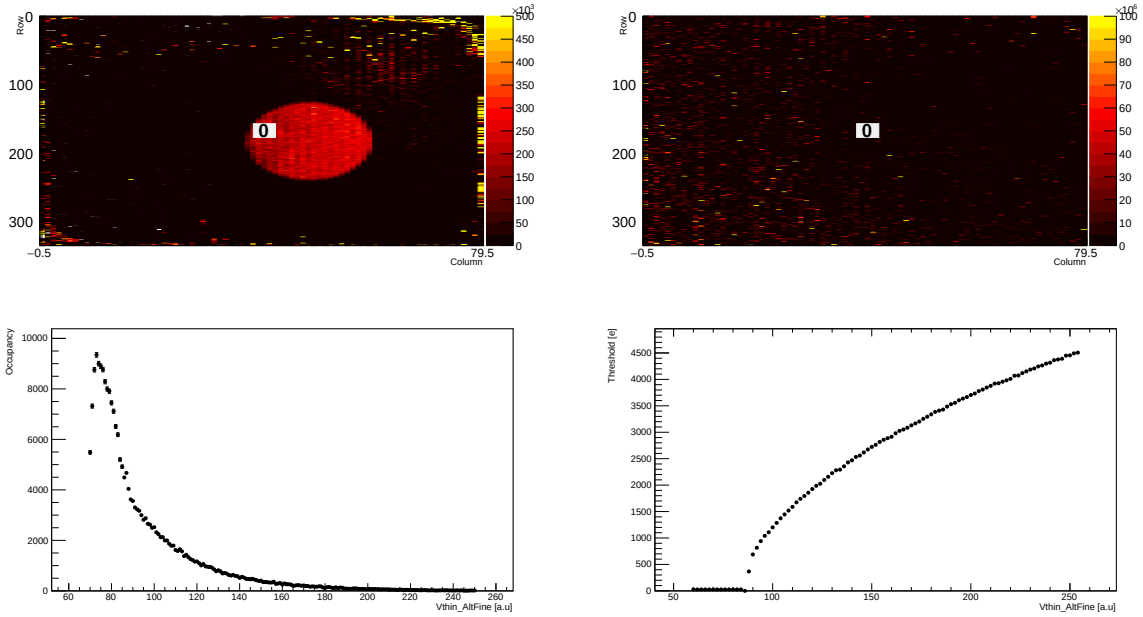

(a) Occupancy as function of GDAC for 25 kV. At the top a map of the occupancy is shown and at the bottom the occupancy of one particular pixel is plotted against the GDAC value.

(b) Threshold against GDAC for standard tuning. At the top a map of the thresholds is shown and at the bottom the threshold found by the threshold scan is plotted against GDAC for one pixel.

Figure 4.16: Example of occupancy as a function of GDAC for Fe and threshold as a function of GDAC for one pixel using the standard tuning.

is the equivalent charge for the Fe lines, and so this measurement provides a lower limit on the offset, in this case, 1780 e.

Nevertheless, it is possible to observe some interesting features in the GDAC offset map. The value of the GDAC offset decreases from left to right in the module. Generally, a spatial effect would be expected. All of the pixels contain the same readout electronics, but there is only one DAC which provides the voltage that is then distributed across the module. This DAC is positioned on the bottom left of the FE (with respect to the map in Fig. 4.17). This means that the distance the signal needs to travel was greater for pixels on the right, and so there were losses for longer wires and thus spatial effects as observed in this measurement.

Measurements with a four chip module

So far, all of the measurements have been completed with one specific module. To check whether the offset is a particular feature of that module or a general FE-I4B property, a different module was used. This time, the four chip module W10-66 was employed,

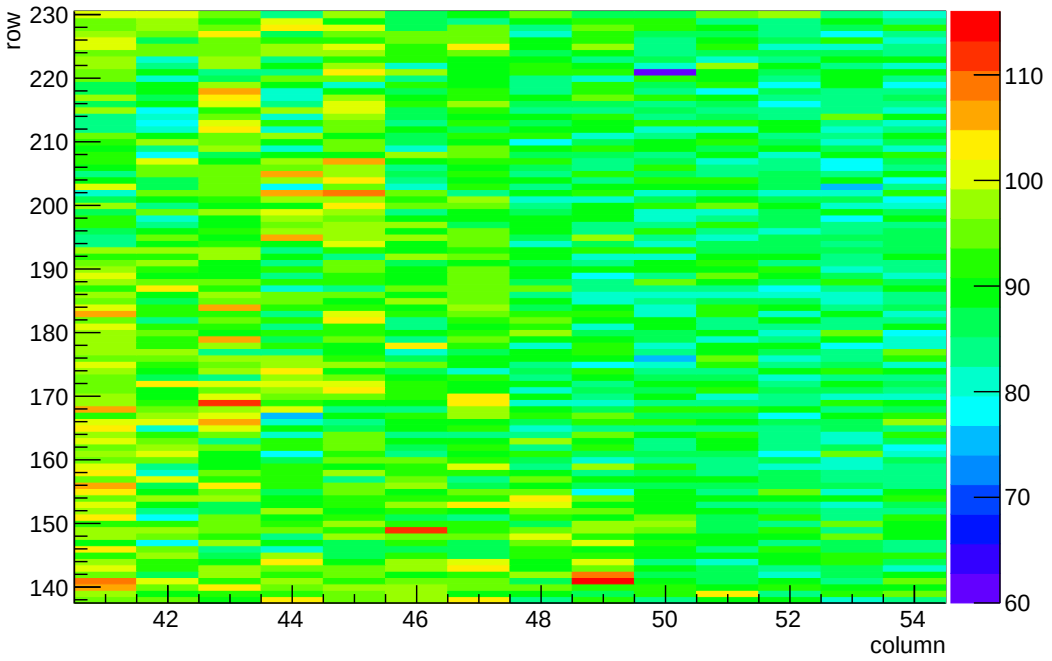

Figure 4.17: Map of the offset for the region of interest that was hit by the beam of the Fe X-ray tube. The colours represent the GDAC offset.

with only one of the modules working. The measurement with the iron X-ray anode was repeated, with the results given in Fig. 4.18. The shape of the occupancy against GDAC measurement appears as expected, with a large decrease at approximately GDAC 90. On the right hand side of Fig. 4.18 a threshold against GDAC measurement is shown. Compared to the single chip module it can be seen that the curve gives non-zero values for higher GDAC values, when compared to the single chip module. This could be due to the fact that the electronics of four chip modules are usually more noisy than those of single chip modules. Unfortunately, this means that this measurement also only provides a lower limit on the offset, corresponding to the equivalent charge of the iron lines, 1780 e.

The GDAC offset analysis can also be performed and leads to the map shown in Fig. 4.19. Again, the offset in GDAC shows a decrease from left to right in the sensor, implying that this is not a feature of one particular module but a general property of the FE-I4B chips.

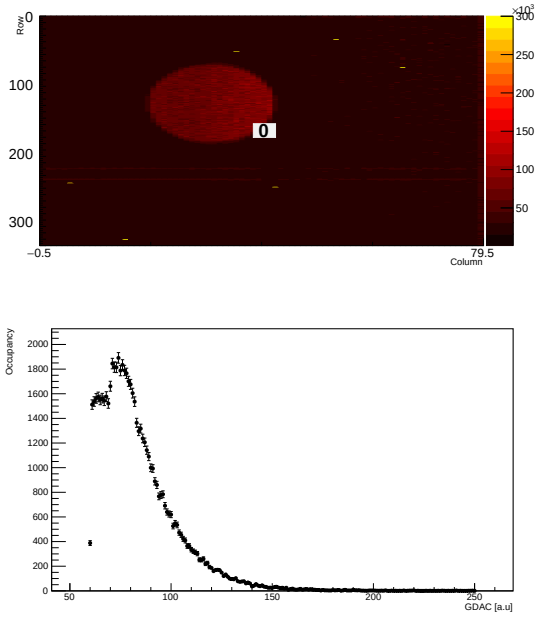

(a) Occupancy as function of GDAC for 25 kV. At the top a map of the occupancy is shown and at the bottom the occupancy of one particular pixel is plotted against the GDAC value.

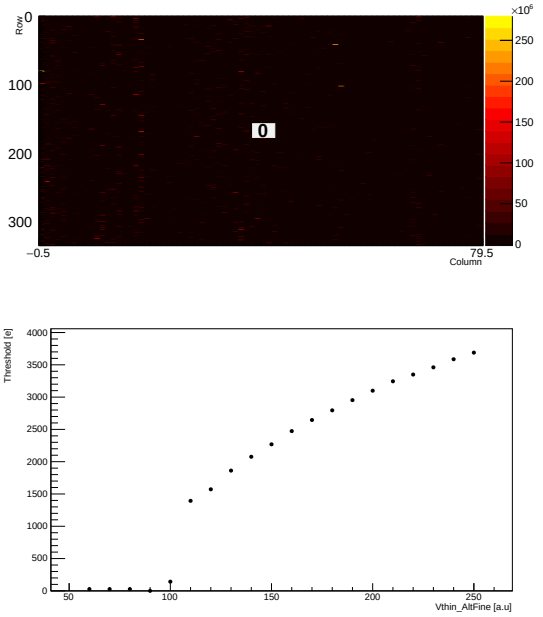

(b) Threshold against GDAC for standard tuning. At the top a map of the thresholds is shown and at the bottom the threshold found by the threshold scan is plotted against GDAC for one ixel.

Figure 4.18: Example of occupancy as a function of GDAC for Fe and threshold as a function of GDAC for one pixel using the standard tuning for the four chip module.

Results for Molybdenum

As the offset appears to be much larger than expected previously, sources with higher energies could be used for a measurement, for example Molybdenum. With the same setup inside an X-ray tube, an occupancy against GDAC measurement can be performed. Instead of using an external trigger, the self trigger of the FE-I4B was used. Previously this was not possible because the occupancy would be too high, as the spectrum of the Bremsstrahlung would account for many hits and the hitbus would be high at all times, which makes it impossible to trigger onto individual hits. This would mean that very few hits would be seen for low GDAC. This is also the reason why in the previous measurements, the occupancy would go to zero for GDAC values below 60. For the self trigger this effect is observed for much larger GDAC values, around 120. Since the region with the X-ray lines of Fe and Cu is far below these GDAC values, the self trigger could not be employed previously. For Mo, the lines are at much higher energies and so at higher GDAC values. Therefore, for Mo it is possible to use the self trigger, which theoretically

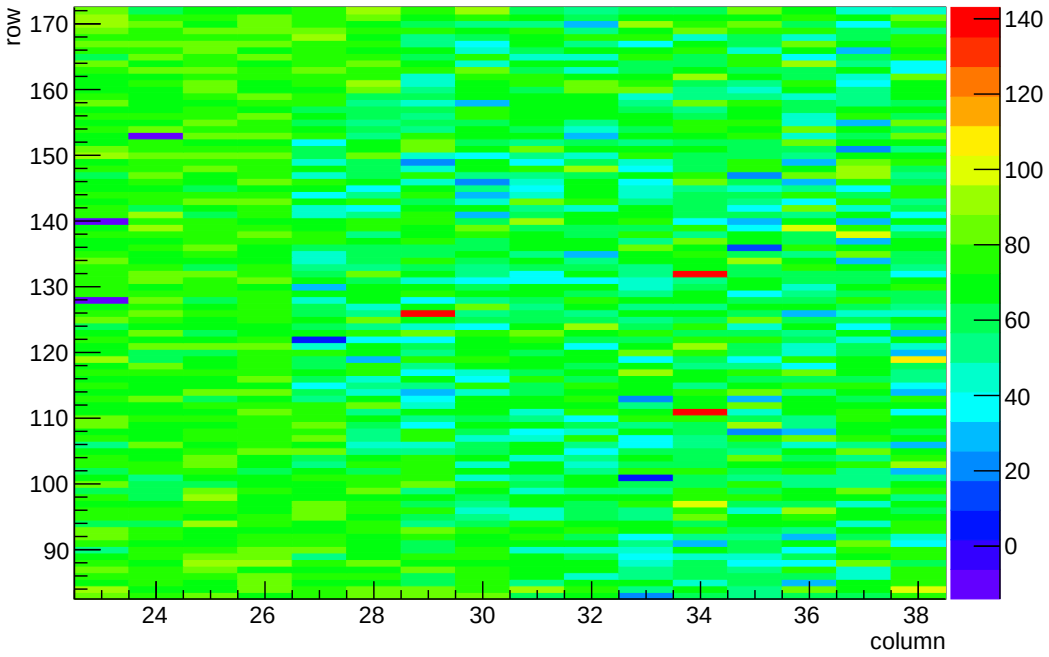

Figure 4.19: Map of the offset for the region of interest that was hit by the beam for the four chip module with the Fe X-ray tube.

registers fewer noise hits. An occupancy against GDAC measurement for Molybdenum is presented in Fig. 4.20 for the single chip module. For this measurement an acceleration voltage of 35 kV was chosen, as the peaks are at much higher energies than for Fe and Cu. In Fig. 4.20, the occupancy is summed over all pixels as the individual pixels did not show the expected pattern as predicted by the measurements for copper or iron. The idea was to get rid of possible stochastic effects by summing over all pixels, but the result still does not provide the expected clear signal.

In order to determine the offset, the charge spectrum of the measurement was used, that can be extracted from the time over threshold information in the raw data of the source scan. The procedure is described in more detail in section 4.2.2. The charge spectrum shows the number of hits with a particular energy/number of charge carriers. When increasing the GDAC and thus increasing the threshold, there should be less charge visible because an increasing fraction of the spectrum will have energies below the threshold. The two main peaks of Mo are at approximately 4800e and so should be visible in the fifth bin of the histograms in Fig. 4.22. The figure shows the charge spectra for different GDAC settings. As expected, the bins with smaller charges are cut off with increasing GDAC values. It is assumed that the threshold is at the position of the Mo lines when the

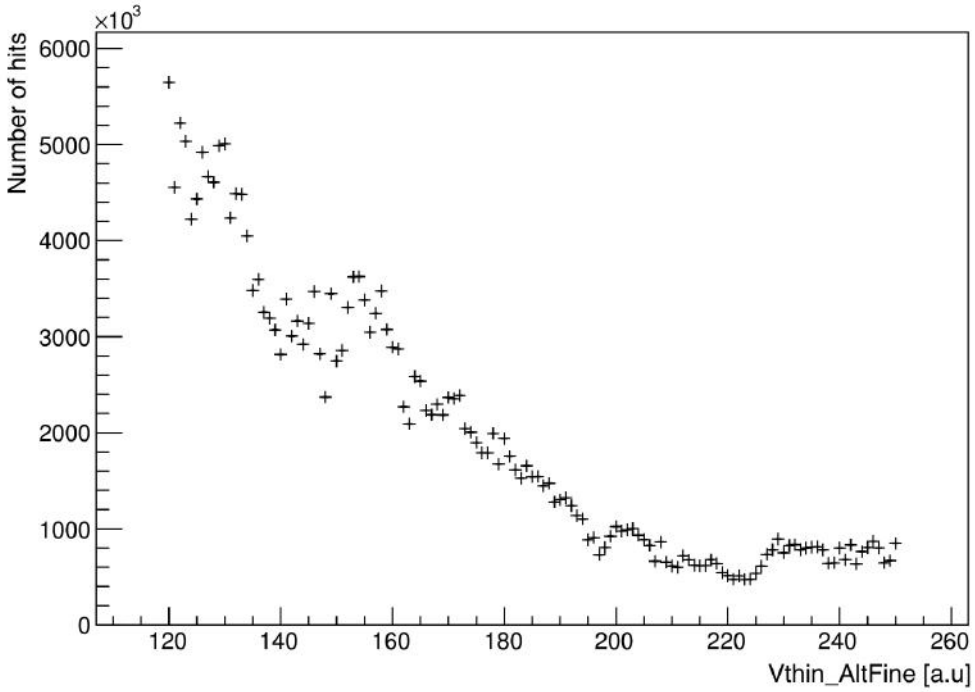

Figure 4.20: Occupancy against GDAC for the Molybdenum X-ray tube at 35 kV, summed over all pixels.

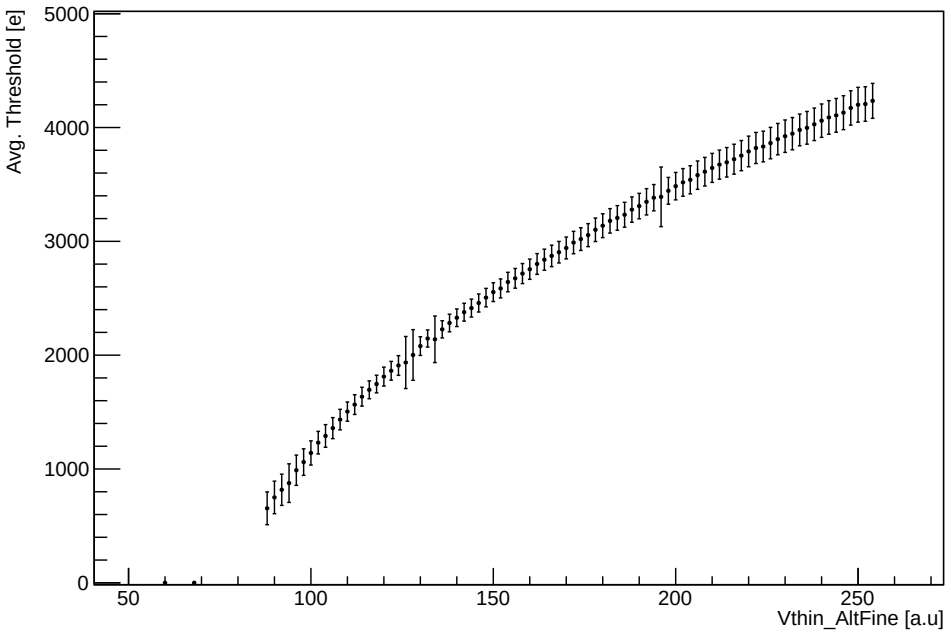

Figure 4.21: Threshold against GDAC averaged over all pixels for standard tuning for the single chip module.

occupancy in the fifth bin (for a signal between 4000 e and 5000 e), has decreased to 50%. This happens between GDAC 150 and 160, so the Mo line is at 155 ± 5. A more precise value can not be found with this data, as the heights of the bins vary for different GDAC values.

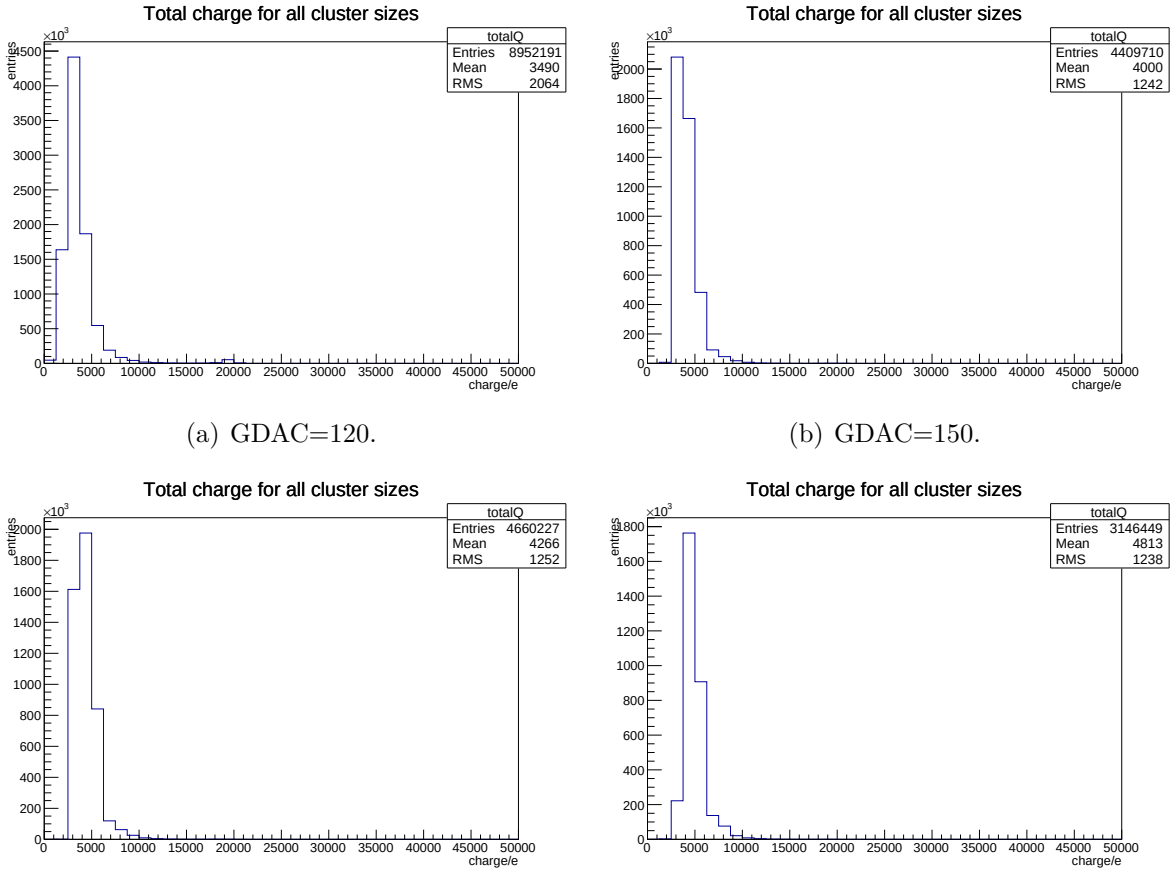

(a) GDAC=120.

(b) GDAC=150.

(c) GDAC=160.

(d) GDAC=180.

Figure 4.22: Charge spectra for different GDAC settings for an X-ray measurement with Molybdenum.

Subsequently, a threshold against GDAC calibration can be used to determine the offset. In Fig. 4.21 it can be seen that the measured threshold value at GDAC 155 corresponds to approximately 2600 e. Considering the errors and a linear fit between GDAC 154 and 156, the measured threshold is (2610 ± 100) e. The average charge of the two lines in the considered bin is (4840 ± 20) e. This means that the offset found in this measurement is (2230 ± 80) e.

The same measurement was repeated for the four chip module. The occupancy against GDAC measurement is presented in Fig. 4.23. As opposed to the previous measurement, the curve shows the expected shape. For this dataset, the individual measurements were

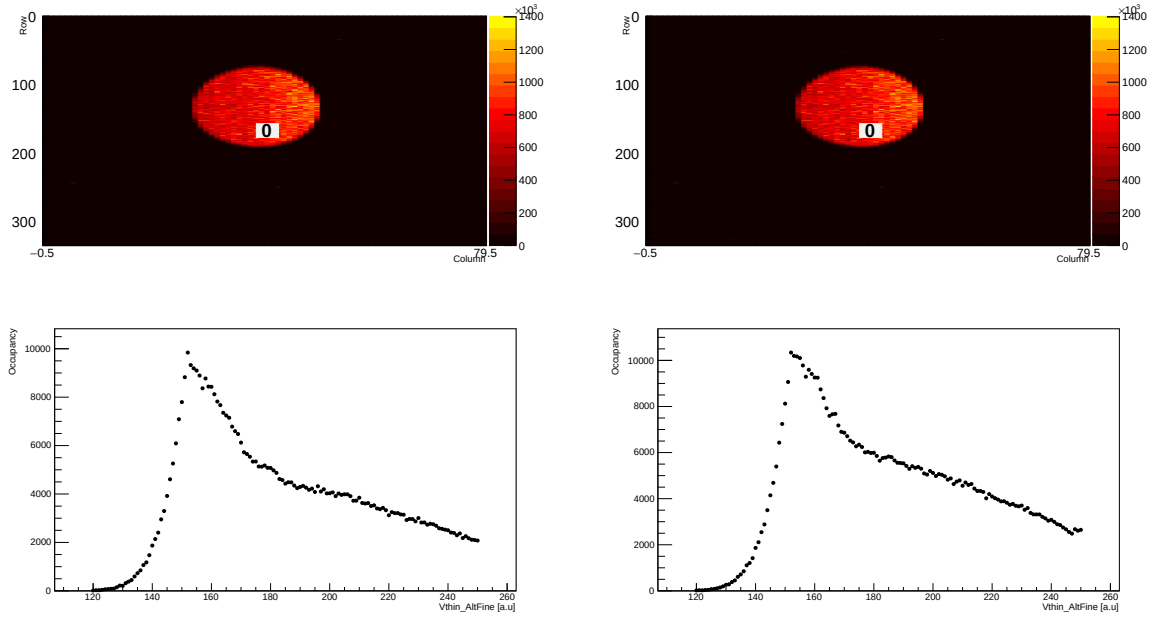

(a) Occupancy as function of GDAC for 35 kV. (b) Occupancy as function of GDAC for 35 kV.

Figure 4.23: Examples of the occupancies as a function of GDAC for two different pixels of the four chip module, which was irradiated with the Mo X-ray tube at 35 kV. At the top a map of the occupancy is shown and at the bottom the occupancy of one particular pixel is plotted against the GDAC value.

performed for twice the duration, a possible explanation for the better data quality. This data allows the same fitting procedures to be utilized as for the iron and copper data. Finding the midpoint of the rapidly decreasing part of the curve and comparing it to the theoretical charge value of the Mo peak leads to the offset map shown in Fig. 4.24. Again, the decrease in offset from left to right can be seen. Averaging over all pixels the offset is (1940 ± 100) e.

4.2.2 Source Measurements

In order to verify the measurements performed with the X-ray tube, a different method of measurement was used. Instead of an X-ray source a radioactive source was used. Again the radiation needs to have a well-defined energy. This is why only sources of gamma radiation were chosen, as the photons always create the same number of electron-hole pairs for the same energy. The available sources that produce gamma radiations are Cd-109 and Am-241. The energies and the equivalent number of electrons are shown in Tab. 4.2.

In comparison to the X-ray tube the radioactive source has a lower intensity, so instead

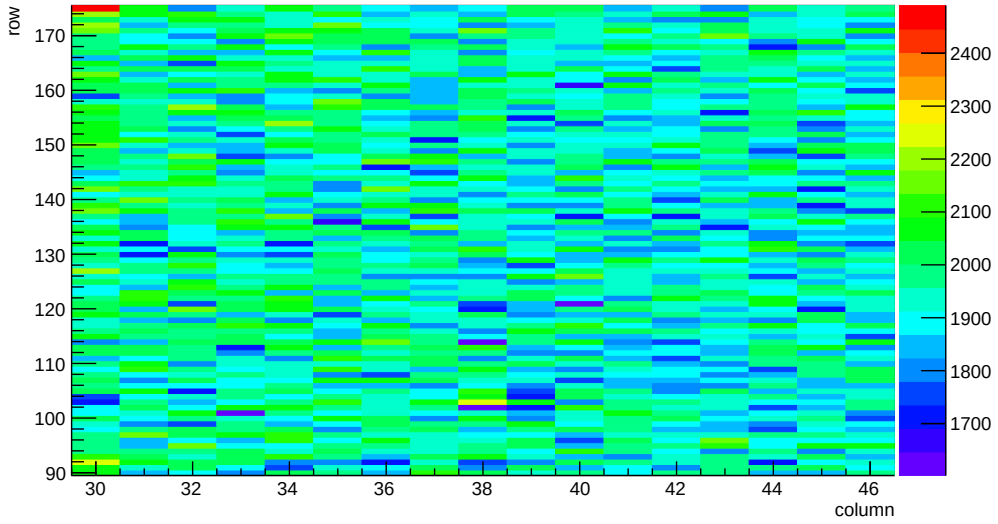

Figure 4.24: Map of the offset for the region of interest that was hit by the beam. Measurement with the four chip module and a Mo X-ray tube. The colours represent the offset in number of electrons.

of using an external trigger, the self-trigger of the FE-I4 was used. Due to the much smaller number of photons, each measurement has to have a longer duration. The individual GDAC scan point took approximately 10 minutes. During this time, only around 10 hits per pixel were registered for the Am-241 source. For the Cd-109 only around 10 hits across the whole sensor were registered during this time. As a consequence, the Cd-109 source was not used for further measurements. For Am-241 not every pixel was analysed individually but instead the occupancy was summed over all pixels. This means that the data also includes the spread of the thresholds across all pixels. To minimise this spread when finding the offset, the Threshold Baseline Tuning was not used, but instead the standard tuning was chosen again, where the spread was much smaller.

Material	Energy [eV]	Number of e
Cd-109	21990	6108
	22163	6156
	88033	24453
Am-241	13810	3836
	18000	5000
	59500	16528

Table 4.2: Energies and deposited charge for different radioactive sources.

For Am-241, the occupancy against GDAC measurement is presented in Fig. 4.25. The occupancy increases closer to the noise floor and decreases for higher GDAC. In between,

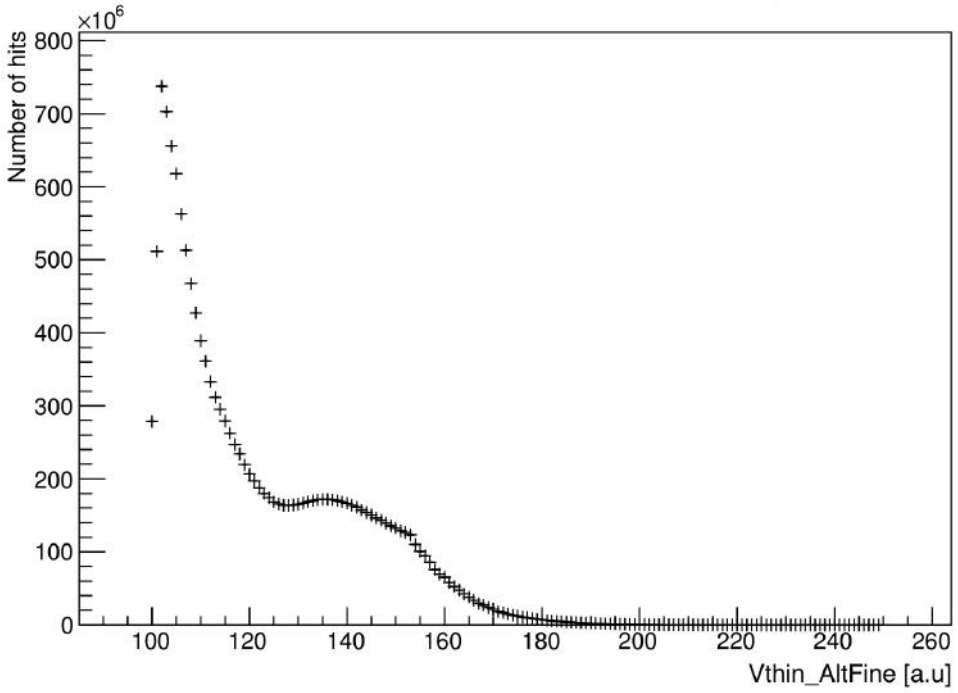

Figure 4.25: Occupancy against GDAC for Americium for the single chip module, summed over all pixels.

there is some unexpected behaviour. At approximately GDAC 120 the occupancy begins to increase again until it decreases again around GDAC 140. Additionally, there is a kink in the curve at around GDAC 160. Due to this, this curve cannot be easily matched to the expected shape, possibly due to the different trigger mechanism or the small number of hits compared to the X-ray measurement.

One possible explanation for the shape of the graph was that some of the signal was lost. If a photon leaves electron-hole pairs in two pixels, it is possible that the signal in one or both pixels is below the threshold and therefore lost. To check this, one can consider the raw data of the source scan, consisting of the Lvl1 and ToT information. The LvL1 value provides information about the time at which the signal was registered after the trigger signal was sent. From the ToT information it is possible to extract a ToT spectrum, which can be transformed into a charge spectrum, using the ToT to charge calibration of the sensor. This spectrum should show the three peaks of the Americium photon spectrum. It is possible to combine hits that are close both in space and time, forming clusters and to consider the ToT spectra for particular cluster sizes. Additionally, it is possible to look at a number of different clusters in one measurement, which can be used to consider whether this might contribute to a loss of signal. This analysis is performed with a ROOT macro,

that, using the parameter files from a ToT calibration scan, returns the data shown in Fig. 4.26.

Firstly, it can be noticed that the LvL1 distribution consists of only two bins, meaning that the signal always arrives after approximately the same duration after the trigger signal has been sent, as would be expected for a self trigger with little noise. The second subfigure shows the number of clusters as a function of clustersize. As can be seen, the vast majority of the clusters have size 1. The number of clusters with clustersize 2 is a factor of 10 smaller, so they should not have a large effect on the measured spectrum. It can still be observed however, that the ToT spectrum for clustersize 2 only contains one peak and not the first Am peak around ToT 3 and 4 as the threshold cuts off the lower energies. The number of clusters with clustersize 3 and 4 can be neglected. At the bottom of Fig. 4.26 the ToT spectrum for all clustersizes and the charge spectrum are shown. Within the charge spectrum, two peaks can be seen. The first peak is a combination of the 14 and 18 keV peaks and the second one is the 59 keV peak. Notably, the 59 keV peak is at a lower charge than expected, due to a scaling issue in the conversion from ToT to charge that is currently being worked on.

The charge spectra for different GDAC values can be used to find the offset. The Am peak at 14 keV should contribute to the third and fourth bins of the histogram. Therefore, due to the nature of the S-curve of the threshold, the number of hits should fall to 50% of its initial value when the threshold is at the value of the first Am peak, 3836 e. This is the case for GDAC $= 145 \pm 5$, as can be seen from Fig. 4.27. Again considering the threshold to GDAC calibration in Fig. 4.21, GDAC 145 should have a threshold of (2410 ± 80) e, leading to an offset of (1430 ± 80) e.

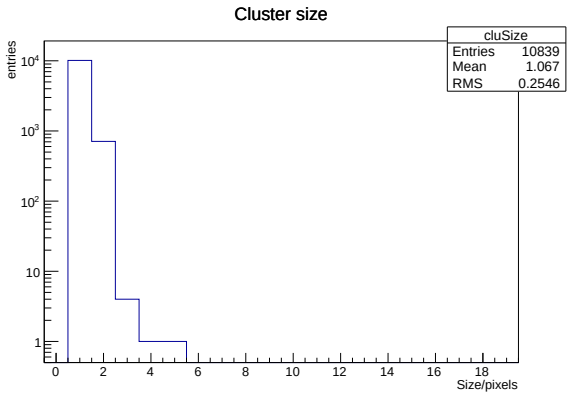

(a) Number of Clusters.

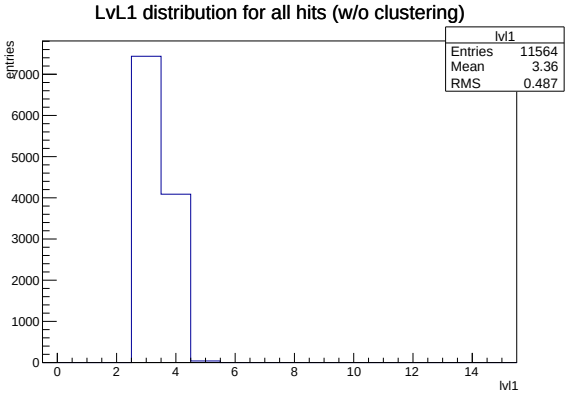

(b) Lvl1 distribution.

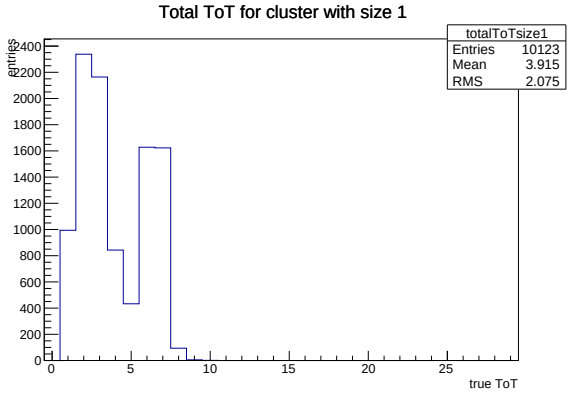

(c) ToT for clustersize 1.

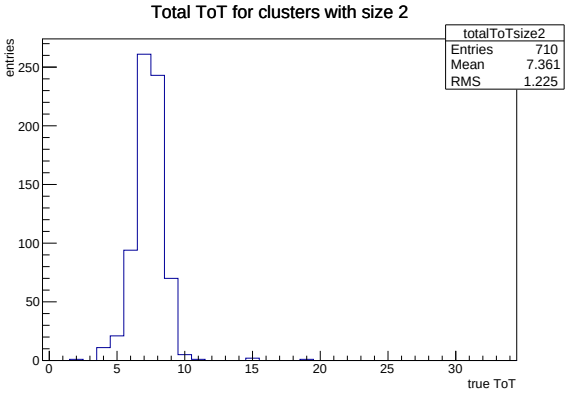

(d) ToT for clustersize 2.

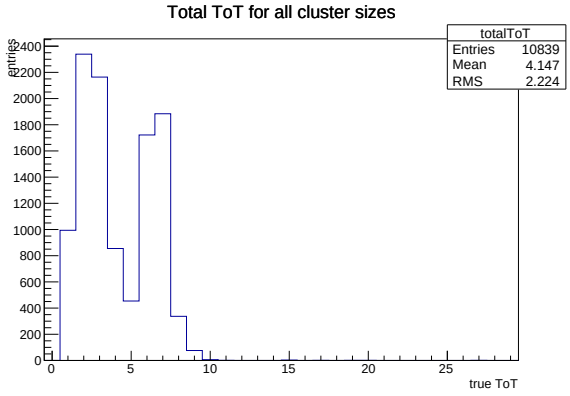

(e) ToT spectrum for all clustersizes.

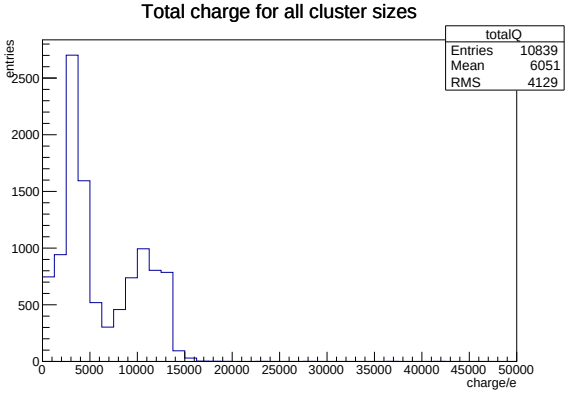

(f) Charge spectrum.

Figure 4.26: Cluster analysis for GDAC=140 for the Am-241 source.

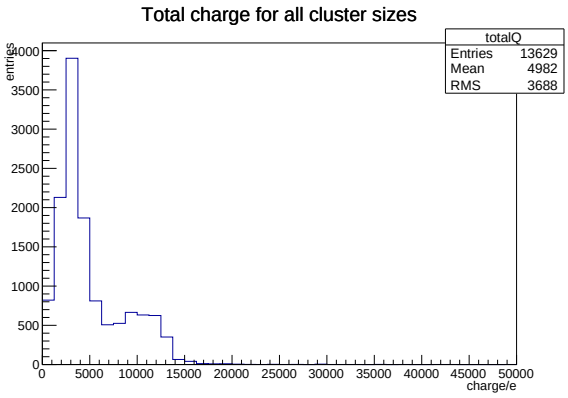

(a) GDAC=100.

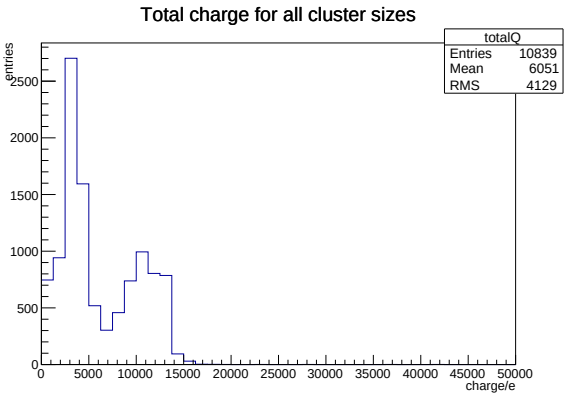

(b) GDAC=140.

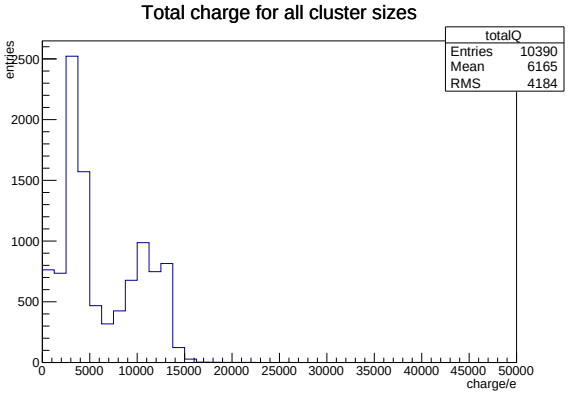

(c) GDAC=143.

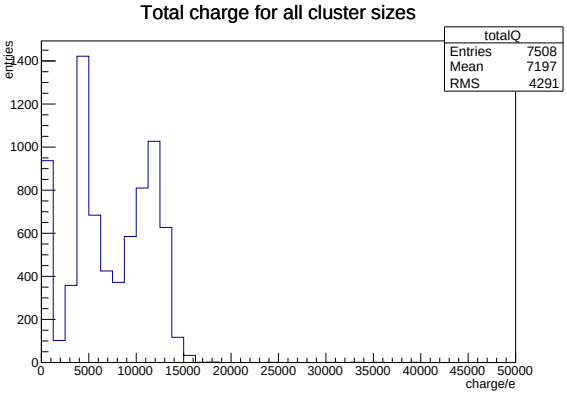

(d) GDAC=145.

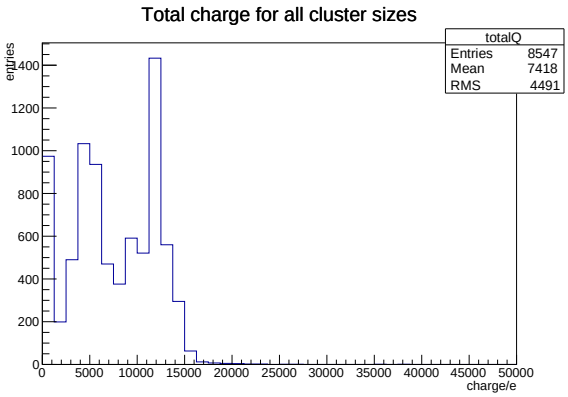

(e) GDAC=180.

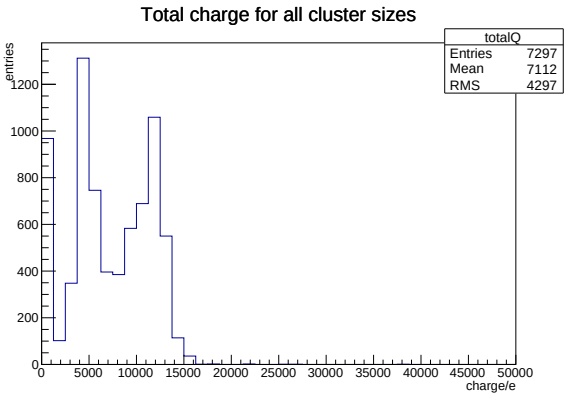

(f) GDAC=200.

Figure 4.27: Charge spectra for different GDAC settings for the Am-241 source.

4.2.3 Combined Results

A combination of all offset measurements is presented in Fig. 4.28. The first two data points are simply lower limits as the threshold scans do not provide a reference point. The two measurements for Molybdenum were made using two different pixels but still give a similar offset value. The offset value for Americium is smaller than the other measurements, though there is no reason why the offset should be constant for different energies.

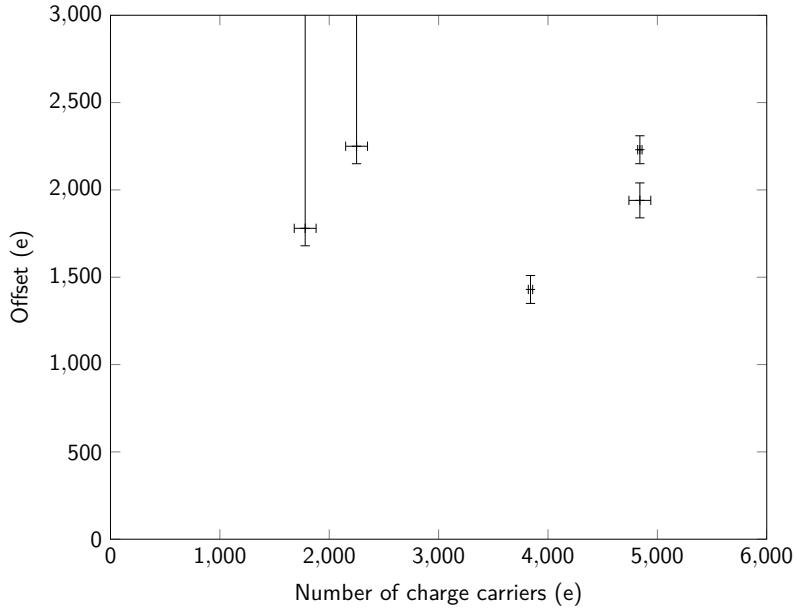

Figure 4.28: Summary of all offset measurements.

Even though the first two measurements only provide a lower limit for the offset they can be used to estimate the threshold reached by the Threshold Baseline Tuning. Each measurement gives a data point that states which GDAC is equal to which threshold. Combining the four different energies at which measurements were made leads to the four data points shown in Fig. 4.29. If the shape of the threshold to GDAC curve looks similar to the one obtained using the threshold scans, the curve should be steeper for low GDAC. From the four data points the shape of the curve cannot be determined, but if a linear function is fitted to the points, the thresholds for GDAC values below 82 (the GDAC value of Fe) should always be below that line. As a consequence, a linear fit provides an upper limit on the threshold reached by the Threshold Baseline Tuning. As mentioned in section 4.1.2, the GDAC value reached by the Threshold Baseline Tuning is 72. With the linear fit in Fig. 4.29 this provides an upper limit of 1570 e on the threshold, with an error of 200 e due to the error in the linear fit.

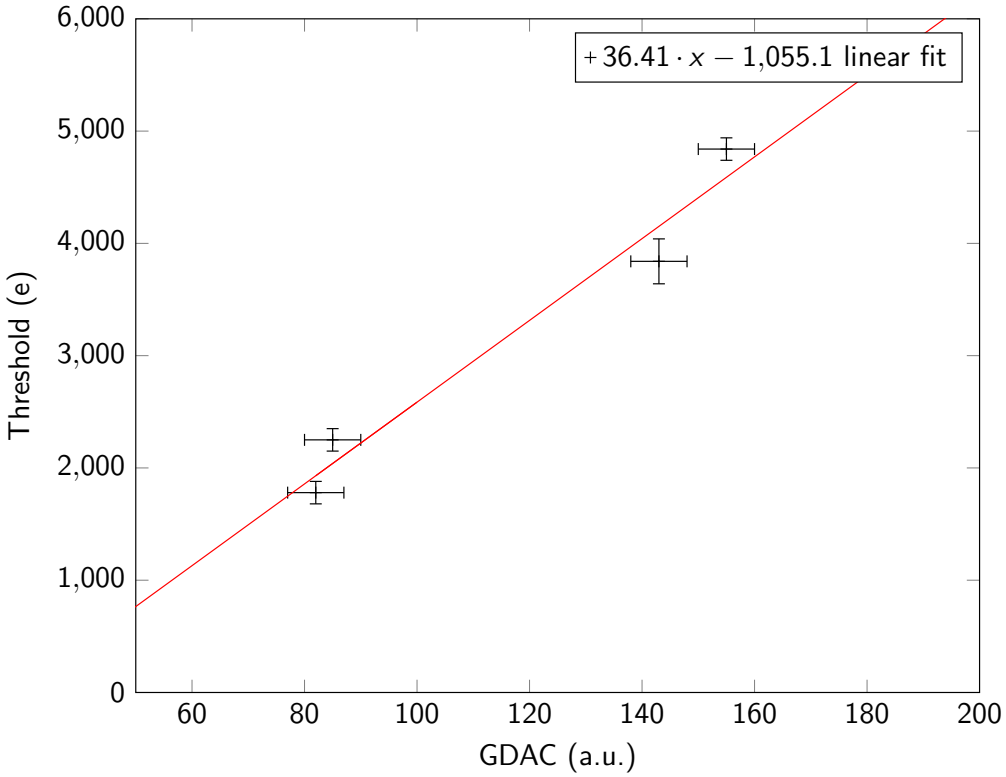

Figure 4.29: Estimation of the threshold for Threshold Baseline Tuning.

5 Summary and Outlook

In this project, the Threshold Baseline Tuning was successfully implemented into STControl. An implementation with a noise occupancy scan and a source scan with external trigger were programmed and compared. This comparison leads to the observation of an offset, introduced by the charge injection electronics, that was much larger than previously expected. As a consequence, multiple measurements were made to determine this offset, using both X-ray sources and gamma sources. The results showed an offset of approximately 2000 e but the exact value depends on the energy of the source used and on the noise in the module. The measurements range from (1430 ± 80) e to a lower limit measurement of (2250 ± 50) e. The data was also used to set an upper limit on the threshold reached by the Threshold Baseline Tuning and thus on the noise floor of the sensor. Using measurements at different energies, this upper limit was found to be (1600 ± 200) e, which is a factor of three higher than was previously expected.

In future, the Threshold Baseline Tuning can be used on diamond pixel sensors. But, while the GDAC and TDAC tuning can be done using this algorithm, an FDAC tuning procedure is not yet a part of the baseline tuning. For a complete tuning procedure, this has to be developed in the future. Nevertheless, first tests will be possible as soon as a working diamond sample is available. But also considering other pixel development, the measured offset is an important quantity. Previously, the offset was estimated at a few hundred electrons and was mostly ignored, whilst in reality it is an order of magnitude higher. This can help explain current issues, such as problems with the ToT to charge conversion in the FE-I4B and can have an effect when performing measurements with the FE-I4B in a laboratory setup. Additionally, for the threshold measurements, an X-ray setup was developed that can now be used for test measurements with sensors, providing photons with low energies, close to the threshold of the modules.

Bibliography

[1] ATLAS Collaboration, *Observation of a new particle in the search for the Standard Model Higgs boson with the ATLAS detector at the LHC*, Phys. Lett. **B716**, 1 (2012)

[2] CMS Collaboration (CMS), *Observation of a new boson at a mass of 125 GeV with the CMS experiment at the LHC*, Phys. Lett. **B716**, 30 (2012)

[3] Particle Data Group Collaboration, *Review of Particle Physics*, Chin. Phys. **C40(10)**, 100001 (2016)

[4] O. S. Bruning, et al., *LHC Design Report Vol.1: The LHC Main Ring* (2004)

[5] ATLAS Collaboration, *Physics at a High-Luminosity LHC with ATLAS*, Technical Report ATL-PHYS-PUB-2013-007, CERN, Geneva (2013)

[6] ATLAS Collaboration, *The ATLAS Experiment at the CERN Large Hadron Collider*, JINST **3**, S08003 (2008)

[7] H. Kolanoski, N. Wermes, *Teilchendetektoren: Grundlagen und Anwendungen*, Springer Verlag (2016)

[8] G. Lutz, *Semiconductor Radiation Detectors: Device Physics*, Springer Verlag (2007)

[9] J. Janssen, *Test beam results of ATLAS DBM pCVD diamond detectors using a novel threshold tuning method*, JINST **12(03)**, C03072

[10] J.-W. Tsung, et al., *Signal and noise of Diamond Pixel Detectors at High Radiation Fluences*, JINST **7**, P09009 (2012)

[11] M. Garcia-Sciveres, et al., *The FE-I4 pixel readout integrated circuit*, Nucl. Instrum. Meth. **A636**, S155 (2011)

[12] Z. He, *Review of the Shockley-Ramo theorem and its application in semiconductor gamma-ray detectors*, Nucl. Instrum. Meth. A **463(1-2)**, 250 (2001)

Acknowledgements

First and foremost, I would like to thank Prof. Dr. Arnulf Quadt for the opportunity to complete this project at the II. Institute of Physics, as well as his continuous support and advice over the course of my degree. I would also like to thank Priv.Doz. Dr. Jörn Große-Knetter for agreeing to be the second referee for this thesis and for his help during the project, especially with the X-ray tubes.

Thank you to Dr. Jens Weingarten and Helge Beck for their support and encouragement throughout the duration of the project, as well as the long discussions about my measurements and results, which greatly helped my understanding of pixel sensors. I am particularly grateful for their comments and suggestions while proofreading this thesis. Furthermore, I would like to thank Tobias Bisanz for the clustering code and to Paolo Sabatini for his input during the interpretation of the Americium spectra.

Thank you to all of the members of the II. Institute of Physics for the great atmosphere and for making this period such an enjoyable experience: in meetings, lunch and coffee breaks.

A very special thanks to Alec Granville-Willett for agreeing to read my thesis and his many helpful comments on my English skills or lack thereof.

Finally, I would like to thank my family for always being supportive and taking care of me.

Erklärung nach §13(9) der Prüfungsordnung für den Bachelor-Studiengang Physik und den Master-Studiengang Physik an der Universität Göttingen:

Hiermit erkläre ich, dass ich diese Abschlussarbeit selbständig verfasst habe, keine anderen als die angegebenen Quellen und Hilfsmittel benutzt habe und alle Stellen, die wörtlich oder sinngemäß aus veröffentlichten Schriften entnommen wurden, als solche kenntlich gemacht habe.
Darüberhinaus erkläre ich, dass diese Abschlussarbeit nicht, auch nicht auszugsweise, im Rahmen einer nichtbestandenen Prüfung an dieser oder einer anderen Hochschule eingereicht wurde.

Göttingen, den 30. August 2017

(Maria Mironova)